Applied Catalysis B: Environmental 286 (2021) 119931

Contents lists available at ScienceDirect

Applied Catalysis B: Environmental

journal homepage: www.elsevier.com/locate/apcatb

CO oxidation activity of Pt/CeO_2 catalysts below 0 °C: platinum loading effects

Andrei I. Boronin [a,*], Elena M. Slavinskaya [a], Alberto Figueroba [b], Andrey I. Stadnichenko [a], Tatyana Yu. Kardash [a], Olga A. Stonkus [a], Elizaveta A. Fedorova [a], Valerii V. Muravev [c], Valery A. Svetlichnyi [d], Albert Bruix [b,e], Konstantin M. Neyman [b,f,**]

[a] Boreskov Institute of Catalysis SB RAS, Novosibirsk, Russia
[b] Departament de Ciència de Materials i Química Física and Institut de Quimica Teòrica i Computacional (IQTCUB), Universitat de Barcelona, Spain
[c] Department of Chemical Engineering and Chemistry, Inorganic Materials & Catalysis, Eindhoven University of Technology, Netherlands
[d] Tomsk State University, Tomsk, Russia
[e] Chair for Theoretical Chemistry and Catalysis Research Center, Technische Universität München, Germany
[f] ICREA (Institució Catalana de Recerca i Estudis Avançats), Barcelona, Spain

ARTICLE INFO

Keywords:
Pt/CeO_2
Low-temperature CO oxidation
Single atom
PtO_x
DFT calculations

ABSTRACT

Reducing the operating temperature of oxidation catalysts is important for designing energy efficient processes, extending catalyst lifetime, and abating pollutants, especially in cold climates. Herein, high CO oxidation activity at sub-ambient temperatures is reported for Pt/CeO_2 catalysts with high content of Pt in the form of dispersed Pt^{2+} and Pt^{4+} centers. Whereas the reference 1 wt%Pt catalyst was active for CO oxidation only above 100°C, the 8 and 20 wt%Pt catalysts converted 60 and 90 % of CO, respectively, below 0°C. Ionic platinum was shown to facilitate oxygen release from ceria and lower the light-off temperature of the reaction occurring through the Mars-van-Krevelen mechanism. However, the remarkable activity observed at sub-ambient temperatures for the ≥8 wt%Pt catalysts is proposed to involve O_2 and CO reactants weakly adsorbed on PtO_x clusters. The synergies between ionic platinum and nanostructured ceria reported in this work advance the knowledge-driven design of catalysts for low-temperature oxidation reactions.

1. Introduction

Platinum catalysts supported on metal oxides are among the most used for a wide range of oxidation reactions. Platinum is often combined with ceria as a catalyst for such reactions as CO oxidation [1–3], CO preferential oxidation [4–7] and water-gas shift [8–12]. Platinum and ceria are also essential components of three-way conversion catalysts (TWC) for the neutralization of automotive exhaust gases [1,13–15]. The oxidizing ability of these catalytic materials can be modified due to the effect of strong metal–support interactions (SMSI) [16–21].

Metal nanoparticles (NPs), even highly dispersed ones, are not the most cost-efficient form of platinum for the generation of surface active sites [22]. It is more beneficial to place atomically dispersed active component on the surface of oxide supports. In this way the expensive platinum can be used to the maximum extent and significant promoting effects can furthermore be achieved due to SMSI. The catalytic efficiency of dispersed Pt present in ionic form at the surface of ceria was first demonstrated by Bera et al. [23] and Fu et al. [24].

The state and structure of active platinum-group metal (PGM) species in PGM/CeO_2 catalysts for low-temperature oxidation (LTO) of CO are of key importance. These species can be *i*) metallic NPs/clusters, *ii*) metal-oxide NPs/clusters and *iii*) neutral/ionic atomically dispersed species. The high activity of catalysts containing substitutional solutions and/or joint phases of PGMs and such reducible oxides as ceria is well documented [25–27].

In catalysts with atomically dispersed Pt on CeO_2 Pt^{2+} cations are preferentially located at the surface of ceria, without forming bulk solid solutions [28]. This is related to the stabilization of Pt^{2+} ions within square-planar [PtO_4] moieties on the surface of nanostructured CeO_2, which is stronger than the stabilization of Pd^{2+} ions [29,30]. Due to such

* Corresponding author at: Boreskov Institute of Catalysis SB RAS, Novosibirsk, Russia.
** Corresponding author at: Departament de Ciència de Materials i Química Física and Institut de Quimica Teòrica i Computacional (IQTCUB), Universitat de Barcelona, Spain.
E-mail addresses: boronin@catalysis.ru, boronin@catalysis.nsk.su (A.I. Boronin), konstantin.neyman@icrea.cat (K.M. Neyman).

https://doi.org/10.1016/j.apcatb.2021.119931
Received 5 October 2020; Received in revised form 14 January 2021; Accepted 18 January 2021
Available online 24 January 2021

strong stabilization, Pt/CeO_2 catalysts with low Pt loading < 1 wt%Pt are stable at calcination up to 800 °C [31–34]. Nevertheless, the state of platinum-ceria in CO oxidation catalysts is still disputed. For instance [35–40], ~1 wt%Pt loading in ceria did not result in catalyst for LTO of CO: the catalyst became active only at 130 °C. At 200 °C the turnover frequency (TOF) of such catalyst was $0.4 \times 10^{-3} s^{-1}$ [38]. There, Pt was characterized as metallic (~2 nm large particles) and ionic (Pt^{2+}). At variance with the 1 %Pt/CeO_2 catalysts, 1 %Pd/CeO_2 catalysts with Pd present only in the 2+ state are active for LTO of CO [27,41–44].

It was assumed that lower activity of Pt/CeO_2 catalysts observed after their oxidative treatment is associated with increased coordination of Pt atoms [45]. In fact, lower coordination of Pt atoms in sub-nanometer PtO_x clusters on CeO_2 can significantly increase the CO oxidation activity of Pt/CeO_2 catalysts [45]. The formation of metallic sub-nanometer clusters in the Pt/CeO_2 systems from single-atom (SA) Pt^{2+} centers under reductive treatment by H_2, CO, etc. [34,46–48], leads to increased oxidative catalytic activity. Reductive treatments enhance activity by enabling the activation of O_2 on oxygen vacancies on ceria [34]. Formation of the vacancies is proposed to be facilitated by Pt^{2+}-SA centers via oxygen transfer to metallic Pt, where adsorbed CO efficiently reacts with O [34]. Pt clusters were also formed on CeO_2 due to platinum segregation during annealing at about 900 °C in air [46], and more recently, the reversible formation of such Pt particles under CO oxidation reaction conditions has been reported by in situ spectroscopy [49]. Thermal treatment under reducing conditions at 500 °C leads to the formation of relatively large Pt particles (3–10 nm) on CeO_2. It was concluded [47,48] that the formation of Pt particles with an optimal size of about 1.4 nm after activation with hydrogen is one of the decisive factors for achieving maximum catalytic activity for CO oxidation. This is consistent with the results of Ding et al. [50] that only Pt NPs are active in CO oxidation, while Pt^{2+}-SA behave as spectators. However, these highly active small Pt particles are unstable and readily transform into Pt^{2+}-SA species in the presence of oxygen at room temperature [34].

The cost/efficiency optimization of Pt/ceria catalysts starting from materials featuring Pt-SA centers appeared to be advantageous [31–34, 51–57]. For instance, Wang et al. [56] reported that Pt-SA centers on ceria serve as seeds to form small PtO_x clusters containing Pt-O-Pt sites. These sites were two to three orders of magnitude more active in catalyzing low-temperature CO oxidation under oxygen-rich conditions than the Pt-SA precursor in Pt_1/CeO_2.

The above-mentioned publications show that after oxidative treatment platinum is present in ceria-supported catalysts as small PtO_x clusters or single atoms (ion Pt^{2+}-SA) in a square-planar coordination PtO_4. However, the structure and oxidation state of platinum under reaction conditions are still debated. Reductive treatment is believed to result in Pt NPs [33,34,47,48] and PtCe NPs [58], although high CO pressures can also cause decomposition of Pt NPs into atoms [59,60] or reduction of Pt^{2+} species to atomic Pt° and Pt^{+} [61]. Partially negatively charged Pt particles located near oxygen vacancies have been also proposed [62], leading to activity increase. Partial reduction of PtO_x clusters on ceria nanowires was also reported to increase catalytic activity towards CO oxidation [45], pointing to the relevance of undercoordinated sites of PtO_x clusters for low-T CO oxidation. A recent review by Liu and Corma [63] extends this brief summary of the variety of Pt species found in Pt/CeO_2 catalysts for CO oxidation, including single atoms, clusters and NPs.

Commonly, Pt/CeO_2 catalysts contain very little Pt and details of the Pt loading effects are not yet well-understood. In this regard, of special interest is the study by Liu et al. [39]. There, CO oxidation activity at 40 °C increased with increasing Pt loading in Pt/CeO_2 catalysts from 0.3 to 10 wt%, with TOF values rising from ~20 to 76 ($\times 10^{-3}$ s^{-1}). Note, however, that specific reaction rates decreased with increasing Pt loading, mainly due to fewer exposed surface Pt sites. At room and lower temperatures these catalysts were inactive.

An interesting aspect of studying Pt/CeO_2 catalysts with varied Pt loading is related to the opportunity of observing (and evaluating the properties of) the full range of common Pt states, i.e. Pt^{4+}, Pt^{2+} and Pt^0, in the resulting material. Understanding the roles of all Pt species and ceria and the synergies between them is expected to extend the design principles for engineering new materials for oxidation reactions at very low temperatures.

This work therefore deals with Pt/CeO_2 catalysts with Pt loading ranging from 1 to 20 wt%. We assess the catalytic performance for CO oxidation through a series of temperature programmed reactions (TPR), determine the state of Pt and ceria components in these materials using X-Ray Photoelectron Spectroscopy (XPS), and elucidate the general structure of the catalysts using Transmission Electron Microscopy (TEM), all while focusing in the intricate effects of platinum-ceria interaction. We also use electronic structure calculations to clarify the interplay between ionic Pt species and the oxygen storage/release capacity of the Pt-CeO_2 nanocomposites. Our results demonstrate remarkable growth of the low-temperature CO oxidation activity of the catalysts with growing platinum loading. More specifically, we observed CO oxidation activity at temperatures as low as −50 °C, which to the best of our knowledge has not been reported for Pt/ceria systems [64]. Our findings also disclose the role of Pt^{2+}/Pt^{4+} states and point to the presence and high activity of PtO_x clusters on the surface of ceria in the high CO oxidation performance detected at very low temperatures.

2. Experimental section

2.1. Sample preparation

Pt/CeO_2 samples were synthesized by co-precipitation. For that aqueous solutions of $Ce(NO_3)_3$ of chemically pure grade and commercial Pt(IV) nitrate with a platinum content of 14.69 wt.% were used. The amount of reagents was calculated per 10.0 g of the finished catalyst of the PtO-CeO_2 composition, based on the mass content of Pt 1.4, 11.0, and 21.7 wt.%. For the synthesis of the 1.4 %Pt/CeO_2 samples, 200 mL mixed solution of $Pt(NO_3)_4$ and $Ce(NO_3)_3$ with Pt and Ce concentrations of 0.70 and 40.08 mg/mL, respectively, was prepared immediately before the precipitation. The corresponding concentrations in the mixed solution were 5.50 and 51.44 mg/mL to prepare the 11.0 %Pt/CeO_2 samples and 10.85 and 31.34 mg/mL to prepare 21.7 %Pt/CeO_2 ones.

A solution containing a mixture of Pt^{4+} and Ce^{3+} nitrates was added drop-by-drop in water (120 mL) at the rate of 12 mL/min under vigorous stirring simultaneously with dropwise addition of 1 M KOH to maintain pH = 8.8−9.0. The obtained precipitate was aged for 2 h before filtering. The samples were first dried at room temperature for 12 h and then for 16 h at 110 °C followed by calcination in air at 450 °C for 4 h. The samples were washed from potassium ions in 500 mL of water with vigorous stirring of the suspension for 30 min, followed by the catalyst separation by filtration. This washing operation was repeated three times. The resulting catalysts were dried in air for 12 h at room temperature and for 16 h at 110 °C. Then the samples were calcined in air at 600 °C for 4 h. The Pt content detected by atomic absorption was 1.1, 8.3 and 20.3 wt% (see Table 1). The corresponding samples are denoted $1Pt/CeO_2$, $8Pt/CeO_2$ and $20Pt/CeO_2$.

2.2. X-ray photoelectron spectroscopy

X-ray photoelectron spectra (XPS) of powder samples were recorded on a KRATOS ES-300 electron spectrometer using MgK_α radiation ($h\nu$ =1253.6 eV). The source power was 70 W. The diameter of the X-ray beam was approximately 8 mm. The samples for analysis before and after the catalytic tests were mounted on the surface of double-sided carbon sticky tape. No sample reduction was observed during spectra acquisition. The spectrometer calibration was performed using bulk gold ($Au4f_{7/2}$) and copper ($Cu2p_{3/2}$) photoelectron lines with binding-energy (BE) values of 84.0 and 932.7 eV, respectively [65]. The position of the Ce3d line at 916.7 eV was used as a standard reference for calibration of

Table 1
Characteristics of the Pt/CeO_2 catalysts.[a]

Pt loading		S_{sp}, m^2/g	XRD			TEM CeO_2 particle size, nm	XPS surface element composition	
wt.%	at.%		CeO_2 lattice parameter, Å	CSR, nm	e_0		Pt. at%	Pt/Ce
1.1	0.33	93	5.414 (1)	8.6 (3)	0.10 (2)	5–10	0.3	0.006
8.3	2.59	134	5.422 (3)	5.9 (6)	0.16 (6)	5–10	2.1	0.05
20.3	6.97	98	5.423 (3)	4.7 (3)	0.17 (8)	3–5	3.6	0.10

[a] S_{sp} – specific surface area; CSR – coherent-scattering region; e_0 – microstrain parameter; values in parentheses means inaccuracy in the last digit.

the spectra [66]. To determine the level of surface contamination, high-sensitivity survey spectra were recorded. The O1s, Ce3d, C1s and Pt4f spectral regions were measured to characterize the charge states of the corresponding elemental species. Chemical composition was calculated from XPS data accounting for atomic sensitivity factors [67]. The *XPSCalc* software was employed for deconvolution of experimental spectra into individual components. This software was previously applied for different samples, including Pd/CeO_2, Pt/CeO_2 catalysts and PtO_x NPs [43,68,69]. The Shirley model and Gauss-Lorentz functions were used for background subtraction and curve fitting, respectively. Before the curve fitting, all experimental spectra were smoothed using a Fourier filter. No considerable difference between the smoothed and experimental curves was observed; the mean-square deviation was less than 1 %.

Ex situ XPS temperature programmed CO reduction (TPR-CO, *ex situ* XPS) experiments were performed in VG ESCALAB HP photoelectron spectrometer equipped with analytical and preparation chambers. The sample pellet approx. 0.2 g with size 7 × 15 mm was resistively heated using a tantalum sample holder. Temperature was controlled with 1 °C precision using chromel-alumel thermocouple mounted on the back side of the pellet and a self-made thermoregulator. The heating and cooling rate was set to 1 °C/s. During the TPR-CO *ex situ* XPS experiment the sample was heated step by step up to 25, 50, 150, 200, 250, 300, 350, 400, and 450 °C for 10 min in a CO atmosphere (p(CO) = 200 Pa that equals to CO pressure in TPR-CO experiments in the flow reactor described below). After each step the sample was cooled to the room temperature, pumped-out in the preparation chamber to high vacuum and moved to analytical chamber for XPS analysis.

2.3. X-ray diffraction

X-ray diffraction (XRD) data were measured using a Bruker D8 diffractometer (CuK_α radiation, λ = 0.154184 nm) with Bragg-Brentano focusing geometry: A multistrip LynxEye (Bruker) detector was applied for signal acquisition. The patterns were measured with a step of 0.05° and a collection time of 3 s per point. Profile analysis was performed employing the TOPAS program and the fundamental parameter approach for describing an instrumental broadening [70]. The PDF-2 Release 2009 database of the International Centre for Diffraction Data (ICDD PDF-2) was used for phase composition analysis (CeO_2 (ICDD PDF-2 #00-043-1002), Pt (ICDD PDF-2 #00-004-0802)).

2.4. Raman spectroscopy

Raman spectra were measured using inVia Basis Raman microscope (Renishaw, U.K.) in the range of 100–2500 cm^{-1} (the spectral range of 250–900 cm^{-1} is presented in Fig. 1d). The 1200 lines/mm diffraction grating provided a spectral resolution not worse than 2 cm^{-1} in the entire range. The second harmonic of a solid-state Nd:YAG laser with a wavelength of 532 nm and a maximum power of 100 mW was used as radiation. A Leica DM 2500 M microscope (Germany) with a 50× objective provided a spatial resolution not worse than 2 μm. To exclude the samples damage during the measurements, 5 % of the laser power was used. To obtain high-quality spectra, the signal was collected for 400 s.

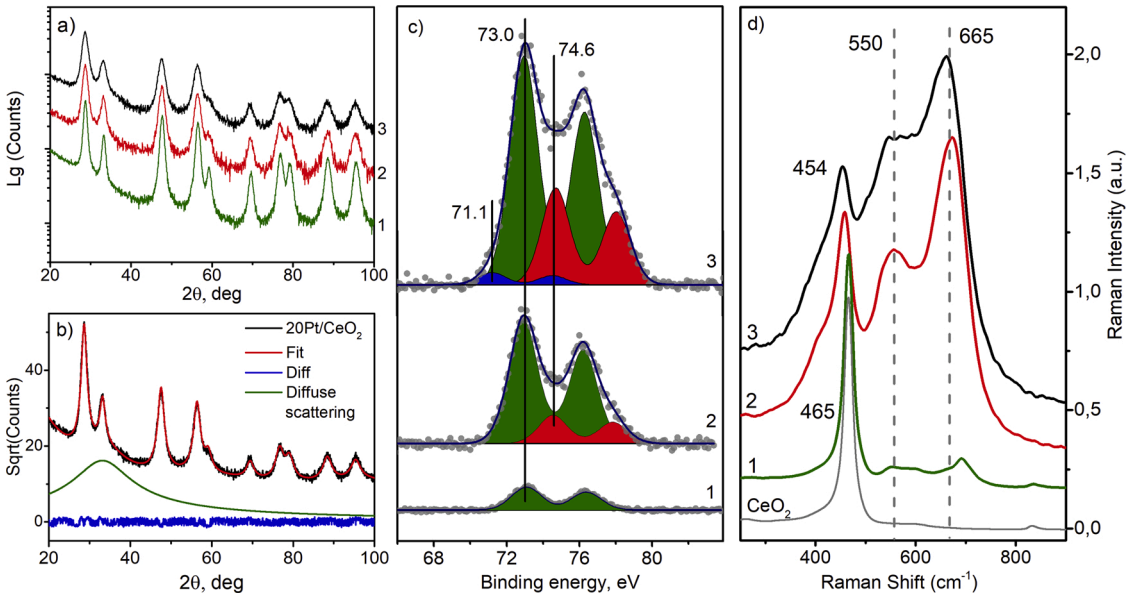

Fig. 1. X-ray patterns (a, b), fitted XPS Pt4f spectra (c) and Raman spectra (d) of the as-prepared **1** - 1Pt/CeO_2, **2** - 8Pt/CeO_2 and **3** - 20Pt/CeO_2 samples. Along with the fitted experimental diffraction pattern for the 20Pt/CeO_2 sample, a broad peak of additional diffuse scattering is shown (b). The Y axis in (a) is in the logarithmic scale, while in (b) it is in the square-root (Sqrt) scale. The peaks of Pt^{2+}, Pt^{4+} and metallic Pt are colored in green, red and blue, respectively (c). Raman spectrum of a pure CeO_2 sample is shown as a grey curve (d). (For interpretation of the references to colour in this figure legend, the reader is referred to the web version of this article.)

2.5. Transmission electron microscopy

The particle morphology was studied by high-resolution transmission electron microscopy (TEM) using a JEM-2010 (JEOL Ltd., Japan) microscope with a lattice resolution of 0.14 nm and accelerating voltage of 200 kV. JEM-2200FS (JEOL Ltd., Japan) electron microscope operated at 200 kV was used for STEM HAADF mode employed together with Energy-Dispersive X-Ray (EDX) spectroscopy. The crystal lattice images were analyzed by the Fourier method. Ca. 10 nm thick carbon films fixed on a standard copper grid were used as substrates.

2.6. Catalytic activity measurements

The CO oxidation activity of the synthesized samples was tested in a flow reactor using the temperature-programmed reaction (TPR-CO + O_2) method during heating, cooling and second heating [27,71]. The samples of volume ~0.25 cm^3 and mass 0.4 g were heated at a rate of 10 °C/min from -10 to 450 °C. The reaction mixture of the composition 0.2 % vol. CO, 1 % vol. O_2, 0.5 % vol. Ne in flowing He was fed at a rate of 1000 cm^3/min, which corresponds to the gas hourly space velocity of 240 000 h^{-1}. The concentrations of CO, CO_2, O_2, H_2, H_2O were monitored using a mass-spectrometer measuring data at a frequency of 0.27 Hz. TOF temperature dependencies for 8Pt/CeO_2 and 20Pt/CeO_2 catalysts were calculated with the aid of CeO_2 dilution (see Supplementary Materials, SM). Ne was added to the gas flow as internal standard to decrease experimental inaccuracy in the concentration measurements of reactants and products in reactor.

The reactor scheme is published elsewhere [72]. The catalyst layer is located between two cylinders: one cylinder is the reactor tube (with a diameter of 8 mm), while the other cylinder is the thermocouple pocket (with a diameter of 3 mm). The length of the catalyst layer is 6 mm. In our measurements, the grain diameter d ranged from 0.14 to 0.25 mm. The reactor was cooled by continuously blowing with a stream of air cooled to −20 °C or to −70 °C depending on the type of experiment. To do this, the air flow passed through a spiral tube located in a cryostat bath with a temperature −35 °C or −80 °C, respectively.

2.7. Temperature programmed reduction

TPR-CO curves were obtained using the reaction mixture containing 1.0 vol.% CO, 0.5 vol.% Ne and He. The gas mixture was introduced at a flow rate of 100 cm^3/min to the catalyst sample (0.1 g for 20Pt/CeO_2 and 0.3 g for 1Pt/CeO_2 and 8Pt/CeO_2) in the reactor to -10 °C. As steady-state concentrations of CO and CO_2 were established, the sample was heated to 450 °C at a 10 °C/min heating rate. The concentrations of CO, CO_2, O_2, H_2, and H_2O were monitored during the reaction by a mass-spectrometer measuring data at a frequency of 0.27 Hz. Before each TPR-CO experiment, the catalysts were pre-treated with a 20 %O_2/He gas mixture at 450 °C during 2 h with subsequent cooling in this mixture and purging in helium afterwards.

For comparison of TPR-CO and TPR-CO + O_2 results obtained for the 20Pt/CeO_2 catalyst at the same pressure of CO, the experimental conditions were as follows: CO – 0.2 vol.%, O_2 – 0 (TPR-CO), 1.0 vol.% (TPR-CO + O_2), catalyst weight 0.1 g, flow of reaction mixture 1000 cm^3/min, heating rate – 10 °C/min.

TPR-H_2 curves were obtained using a reaction mixture containing 10.0 vol.% H_2 and helium. Before each TPR-H_2 experiment, the catalysts were pretreated by a 20 %O_2/He gas mixture at 450 °C during 2 h with subsequent cooling in this mixture. Then, the catalyst was purged with helium for 30 min at room temperature to remove O_2 from the gas phase. The reaction mixture was introduced at a flow rate of 100 cm^3/min to the catalysts (0.3 g for 1Pt/CeO_2, 8Pt/CeO_2 and 0.1 g for 20Pt/CeO_2), which were precooled in the reactor to −40 °C. As the steady-state concentration of H_2 was established, the sample was heated from −40 to 450 °C at a heating rate of 10 °C/min. The concentration of H_2 was measured during the reaction.

2.8. Computational details

Spin-polarized density-functional theory (DFT) calculations were performed using the periodic plane-wave code VASP [73,74]. The PW91 exchange-correlation functional [75,76] of the generalized-gradient approximation (GGA) type was used. Stoichiometric and partially reduced ceria can be satisfactorily described with the GGA+U approach introducing on-site Coulombic interaction of Ce 4f electrons. We applied the GGA+U scheme [77] with U =4 eV [78–80], resulting in the PW91 + 4 approach. Interaction between core and valence electrons was accounted *via* the projector-augmented wave (PAW) method [81]. The kinetic energy cut-off for the plane-wave basis was 415 eV.

Pt-doped ceria NPs were based on $Ce_{40}O_{80}$ (1.4 nm large) and $Ce_{80}O_{160}$ (1.9 nm large) model particles [78] with the fluorite crystalline structure of CeO_2. The particles were positioned in the supercells 2.50 × 2.20 × 2.20 nm^3 and 2.65 × 2.65 × 2.75 nm^3 large, respectively. There, inter-particle distances for neighbouring cells longer than 0.7 nm ensured small enough effects on the calculated geometries and energies [82,83]. Doping by Pt was modelled by adsorbing one Pt atom on a surface O_4 site, which anchors very strongly various transition metal atoms (including atomic Pt as Pt^{2+}) [29], in order to account for the smallest concentrations of the dopant, and by substituting one near-surface inner Ce atom with another Pt atom. The resulting nanoparticulate Pt-doped ceria models without oxygen vacancies (O_v) are Pt/$PtCe_{39}O_{80}$ and Pt/$PtCe_{79}O_{160}$, where Pt before (after) the slash denotes the adsorbed (inner dopant) atom. Up to three O_v were created in each of these models by removing O atoms directly surrounding the Pt dopant. Only Γ-point calculations of the finite models were performed.

Calculations of Pt-doped models of CeO_2 bulk were performed for supercells containing 32 Ce and 64 O atoms. The PW91 + 4 optimized ceria bulk lattice parameter 0.547 nm [80] resulted in the cubic supercell dimensions 1.095 nm. A Monkhorst-Pack set of 4×4×4 *k*-points was used. Local positions of all atoms were optimized in the NP and bulk models until forces acting on each atom became <0.2 eV/nm. See more details on the computational method and the structural models used in other studies successfully rationalizing and predicting several experimental observations [22,29,78,79,84–86].

3. Results

3.1. Catalyst characterization

Table 1 lists characteristics of the Pt/CeO_2 catalysts under scrutiny. Their specific surface area S_{sp} is ca. 90−130 m^2/g. Increase of Pt loading from 1 to 8 wt% results in increase of the specific surface area of the samples. Interestingly, the surface area of the 20Pt/CeO_2 sample shrank back, almost to the value of the 1Pt/CeO_2 sample (see more details in Section 3.2).

3.2. XRD, XPS and Raman spectroscopy data

All lines in the XRD patterns (see Fig. 1a) can be attributed to CeO_2 with the fluorite-type structure. There are no peaks that could be assigned to metallic platinum or its oxides. The broadening of XRD peaks and their shifts as Pt content increases indicate the decrease in particle size and changes in a lattice parameter of the fluorite phase.

Structural characteristics of the fluorite phase in the studied samples are shown in the Table 1. Rietveld refinement of the diffraction pattern was applied for profile analysis and calculation of microstructural parameters. For the 1Pt/CeO_2 and 8Pt/CeO_2 samples the experimental diffraction patterns were well described using only the CeO_2 fluorite structure. For the 20Pt/CeO_2 sample the addition of the broad diffuse peak to the refinement of the CeO_2 fluorite structure was necessary to obtain a good fit (see Fig. 1b).

Platinum content increase is accompanied by a gradual size decrease of the ceria coherent scattering region (CSR). The latter shrinks from 8.6

nm for the 1Pt/CeO_2 sample to 5.9 and 4.7 nm for the 8Pt/CeO_2 and 20Pt/CeO_2 samples, respectively. The CSR decrease is not accompanied by the specific surface area increase; on the contrary, the surface area of the 20Pt/CeO_2 sample decreases in comparison to the 8Pt/CeO_2 sample.

An important feature of the XRD pattern of the 20Pt/CeO_2 sample is the presence of an additional big diffuse peak (Fig. 1b). We attribute the presence of this diffuse scattering to a distortion of intergranular boundaries, which connect small crystalline particles to form bigger aggregates. The size of small crystallites is measured by XRD, whereas the surface of big aggregates is measured by nitrogen adsorption (BET method). The formation of such a specific microstructure with highly distorted intercrystalline boundaries explains the shrinking of the specific surface area and the simultaneous decrease of crystallite size.

Changes were also observed in the lattice parameter of CeO_2 (Fig. S1, Table 1). In the 1Pt/CeO_2 sample, it is close to 5.4113 Å for pure ceria [87] (No. 00-034-0394) and increases with platinum content. The lattice parameter increase is typical for the nanocrystalline ceria [88,89], often indicating distortions in the crystalline structure. The microstrain parameter e_0 is also sensitive to the lattice distortion, since it estimates the mean relative deviation of interplanar distances, which increases with growing Pt loading in the samples (Table 1).

Fig. 1c displays XPS Pt4f spectra of three Pt/CeO_2 samples showing that oxidation states of platinum change with increasing its amount in the samples (see also Table S1). The spectrum of the 1Pt/CeO_2 sample features a single doublet; this means that the catalyst contains Pt in only one oxidation state characterized by $E_b(Pt4f_{7/2})$ =73.0 eV, the value typical for Pt^{2+} ions [25,39,40,69,90]. It is somewhat higher than the E_b of Pt^{2+} in PtO oxide [68], possibly due to interaction of Pt^{2+} cations with ceria. The Pt4f spectrum of the 8Pt/CeO_2 catalyst reveals two doublets with $E_b(Pt4f_{7/2})$ = 73.0 and 74.6 eV. The latter feature corresponds to Pt^{4+} [25,69,91]. The Pt4f spectrum of 20Pt/CeO_2 catalyst is also fitted to two main components, $E_b(Pt4f_{7/2})$ = 73.0 and 74.6 eV, revealing an increased contribution of the Pt^{4+} state compared to the 8Pt/CeO_2 sample. A very small amount of metallic Pt is also detected in the 20Pt/CeO_2 sample as a doublet with $E_b(Pt4f_{7/2})$ =71.1 eV, which may result directly from the synthesis or from the action of X-ray flux on the highly active metal-ceria surface [92–94]. Notably (see Fig. S2 and Table S1), the fraction of Ce^{3+} in the catalysts barely changes, regardless of the amount of platinum added. The observed amount of Ce^{3+} is within the limits of the values typical for ceria powder samples.

For uniform platinum distributions at the sample surface, Pt/Ce ratios calculated from XPS results would coincide with the ratios obtained from analytical data. Platinum in subsurface positions or within crystallite boundaries in the support matrix should decrease the XPS Pt/Ce ratios. Indeed (see Fig. S3), in catalysts at increased Pt loading we determined from the XPS data lower Pt/Ce atomic ratios compared to the analytical data. It implies subsurface location of some Pt, not necessarily only inside CeO_2 ordered lattice. We assume that Pt is partly distributed within boundaries of CeO_2 crystallites. The observed distortion of the ceria lattice is also partially due to incorporation of some Pt^{4+} ions there.

In the lowest-percentage catalyst (1 %) the amount of Pt calculated from XPS is close to the loaded amount (Fig. S3). This corroborates the assumption that in this sample Pt is located mostly on the surface of ceria particles. In case of higher-percentage catalysts (8−20 %) the amount of Pt calculated from XPS is lower than that provided by the analytical data. At higher Pt loadings a part of Pt^{2+} cations and most of the Pt^{4+} cations are located in subsurface regions of ceria, which decreases Pt4f intensity at the same Pt amount (Fig. S3). The small fraction of metallic platinum makes an insignificant contribution to the integral Pt/Ce ratio.

Raman spectra of the catalysts samples doped with Pt are shown in Fig. 1d in comparison with the spectrum of pure polycrystalline $CeO_{2\text{-support}}$. In the latter, in addition to the F_{2g} band at 465 cm^{-1}, weak vibrations at 260 and 320 cm^{-1} are related to longitudinal and transversal stretching modes of ceria [95]. A very small peak at 832 cm^{-1} is visible in the spectra of bare ceria and the 1Pt/CeO_2 catalyst but not of the 8Pt/CeO_2 and 20Pt/CeO_2 catalysts. This peak can be assigned to peroxide species O_2^{2-} adsorbed on ceria surface vacancies [95]. CeO_2 is also characterized by a wide disorder band (D band) around 500−650 cm^{-1} [96]. The D band is very sensitive to defects in the CeO_2 structure, especially those arising upon doping [96–98]. At the lowest level of doping (sample 1Pt/CeO_2) position of the main F_{2g} band related to the tension vibrations of oxygen atoms surrounding cerium atoms in cubic fluorite type structure of CeO_2 remains unchanged, at ~465 cm^{-1}. Pt loading increase leads to broadening of the F2g band and its shift to lower frequencies, 458 and 454 cm^{-1} for the 8Pt/CeO_2 and 20Pt/CeO_2 samples, respectively. This indicates a CeO_2 particle size decrease and correlates well with the XRD data. In the D band region of 500−750 cm^{-1}, highly intense Raman bands appear around 550 and 665 cm^{-1}. Effects of platinum doping of ceria on Raman spectra have been studied quite well, both experimentally and theoretically [28,98–101]. Broad peaks at 550 and 665 cm^{-1} are usually associated with asymmetric and symmetric vibrations, respectively, of Pt−O−Ce on the surface of mixed oxides [101], which could originate from atomically dispersed Pt^{n+} species or PtO_x clusters. In [98,100], the Raman band in the region around 665 cm^{-1} is referred to the Pt−O complex on CeO_2. No peaks that could be attributed to PtO and PtO_2 oxides were detected in our experiments.

We note that a decrease in lattice parameter is expected upon doping with Pt^{4+} species having smaller ionic radius than Ce^{4+}, as is the case of $Ce_xZr_{1-x}O_{2-\delta}$ systems [102]. However, we only observe the increase in the lattice parameter characteristic of nanosized CeO_2 [88,89]. Although Raman-spectroscopy data and microstrains show the defectiveness of ceria particles due to incorporation of Pt^{4+} into the lattice, the small effect on the ceria lattice parameter and the large Pt/Ce ratios obtained by integrating the XPS spectra indicate that most of the Pt ions in the 20Pt/CeO_2 sample are located at or near the surface of the ceria nanoparticles.

3.3. TEM data

TEM data of 1Pt/CeO_2, 8Pt/CeO_2 and 20Pt/CeO_2 are presented in Figs. 2 and 3. HRTEM images (Fig. 2(a–c)) reveal highly dispersed ceria NPs, whose size decreases with increasing Pt content. CeO_2 particles are 5–10 nm large in 1Pt/CeO_2 and 8Pt/CeO_2 samples, while 20Pt/CeO_2 sample also contains smaller crystallites of 3–5 nm.

Spatial platinum distribution was investigated using Energy-Dispersive X-Ray (EDX) spectroscopy. High Angle Annular Dark Field Scanning Transmission Electron Microscopy (HAADF-STEM) images of 8Pt/CeO_2 and 20Pt/CeO_2 samples are shown in Fig. 2(d, e) along with the corresponding EDX maps for Pt and Ce. As seen in the EDX images, Pt is homogeneously distributed over the entire samples. There are no regions with sufficiently high Pt concentrations that would indicate the presence of large metallic Pt^0 or oxidic PtO_x particles, although the presence of small Pt or PtO_x clusters cannot be discarded on the basis of this data. EDX spectra of 8Pt/CeO_2 and 20Pt/CeO_2 samples are presented in Fig. 2(f)–(g). The atomic platinum content measured from these spectra in the imaged regions is 2.7at% and 7.2at%, respectively, for the 8Pt/CeO_2 and 20Pt/CeO_2 samples. Also, HAADF-STEM results and EDX profile along a selected direction of the 20Pt/CeO_2 sample in Fig. S4 show the presence of Pt in all areas of the probed catalyst. The Pt/Ce atomic ratio in the studied region varies from 0.15 to 0.35, which in addition to XPS data – see Table S1 and Fig. S3 – showing that near-surface Pt/Ce ratio is ca. 0.1, indicates that a high amount of Pt is incorporated in the ceria lattice. For the 1Pt/CeO_2 sample, the integrated EDX content exactly corresponds to the nominal composition.

Thus, the TEM and EDX data agree with the XRD and XPS data concerning absence of noticeable formation of metallic Pt^0 or oxidic PtO_x nanoparticles. However, a question remains concerning formation of small Pt^0 and PtO_x surface clusters. Presence of such clusters can be examined by HRTEM and HAADF-STEM measurements.

HRTEM and HAADF-STEM data in Fig. 3 reveal formation of metallic

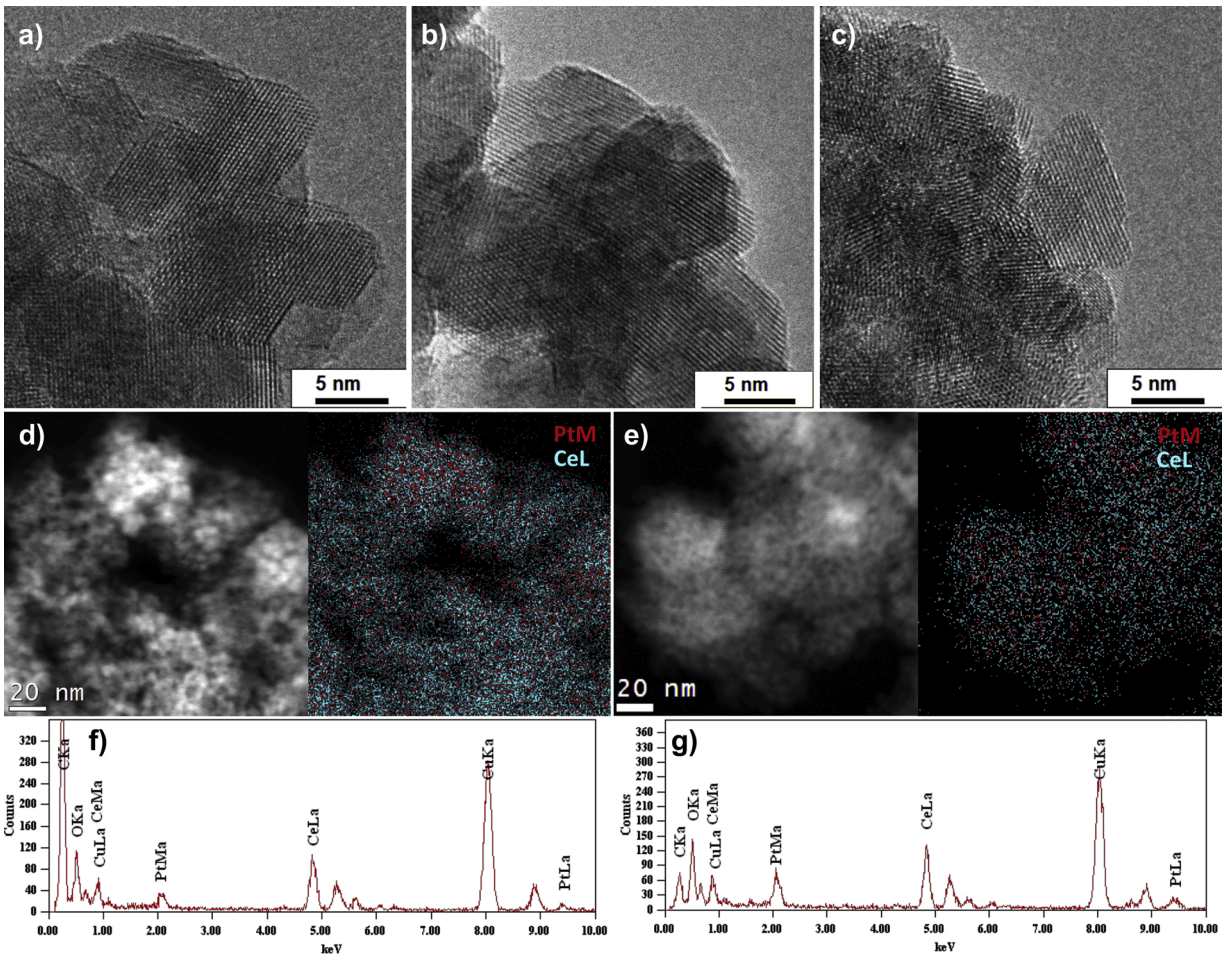

Fig. 2. (a) – (c) HRTEM-images of the 1Pt/CeO_2, 8Pt/CeO_2 and 20Pt/CeO_2 samples; (d) – (e) HAADF-STEM images and corresponding EDX-mapping patterns (Ce L signal is shown in blue, Pt L signal is shown in red) of 8Pt/CeO_2 (d) and 20Pt/CeO_2 (e) samples; (f) – (g) EDX spectra of the 8Pt/CeO_2 and 20Pt/CeO_2 samples, respectively. (For interpretation of the references to colour in this figure legend, the reader is referred to the web version of this article.)

Pt clusters in the 8Pt/CeO_2 sample after redox treatment and under the electron beam action. The redox treatments strongly affect the state of platinum species and lead to formation of metallic Pt clusters and nanoparticles observed all over the ceria surface (Fig. 3b). The investigation of samples after their 1 year exposure to air shows that the electron beam also stimulates the formation of clusters although less intensely than the redox pretreatment does: the clusters, hardly visible at first (Fig. 3c), grow notably under electron beam exposure (Fig. 3d).

The HRTEM and HAADF-STEM images show that high Pt loading facilitates the formation of Pt clusters in Pt/CeO_2 samples. Ionic platinum at such high concentrations becomes unstable under the action of the electron beam and starts to migrate and agglomerate. The instability of platinum species during TEM investigation suggests that the observed cluster forms are not the initial state of the catalyst. At the same time, it does not allow us to obtain demonstrative images of solely ionic platinum forms present. In general, these dynamic processes to form metallic Pt clusters observed by us are structural transformations that also can occur under reaction conditions and affect catalytic properties. However, the high activity of catalysts with high Pt loading cannot be explained by the formation of metallic Pt clusters – these particles do not form at the low temperatures at which high activity is observed and, in addition, metallic Pt particles supported on ceria feature CO oxidation light-off temperatures well above 25 °C [49,103].

3.4. TPR-CO and TPR-H_2 data

Fig. 4a shows CO_2 evolution during TPR-CO (in the absence of the external oxygen supply) for the 1Pt/CeO_2, 8Pt/CeO_2, 20Pt/CeO_2 catalysts compared with pure CeO_2. For the latter, no consumption of CO and evolution of CO_2 is detected below ~200 °C. This indicates that there is no reactive lattice oxygen at these temperatures in the pristine CeO_2 sample. For the 1Pt/CeO_2 catalyst, there are two peaks measured at 115 and 160 °C in the spectra of CO consumption and CO_2 evolution. This suggests that the presence of Pt already at 1 wt% leads to the formation of sites that can bind CO and activate lattice O, and the evolution of CO_2 starts at 90 °C (Fig. S5a). With Pt content increase the onset of CO_2 evolution shifts to lower temperatures of 20 °C and −3 °C for the 8Pt/CeO_2 and 20Pt/CeO_2 catalysts, respectively (Figs. 4a and S5a). The presence of more than one TPR-CO peak indicates that various forms of reactive oxygen are present in the Pt/CeO_2 catalysts, including some in the form of PtO_x clusters. In fact, our TPR-CO data for the 20Pt/CeO_2 catalysts are similar to those obtained by Ke et al. for PtO_x clusters supported on ceria nanowires [45], with light−off temperatures of ~0−25 °C for the catalysts exposing PtO_x clusters.

The amount of oxygen atoms released during the TPR-CO experiments from Pt/CeO_2 catalysts equals to the amount of evolved CO_2 molecules. The latter linearly correlates with the amount of Pt atoms (see Fig. 4b), essentially all being Pt^{2+} and Pt^{4+} cations in the Pt/CeO_2 samples. The slope value ~2 manifests that on average ca. two oxygen atoms are released from the vicinity of each platinum cation.

Fig. S5b displays the temperature dependences of hydrogen consumption by the catalysts with different Pt content. For the pristine CeO_2 support, hydrogen consumption starts at a temperature above 300 °C [28], which is in agreement with literature data [39,93]. For the

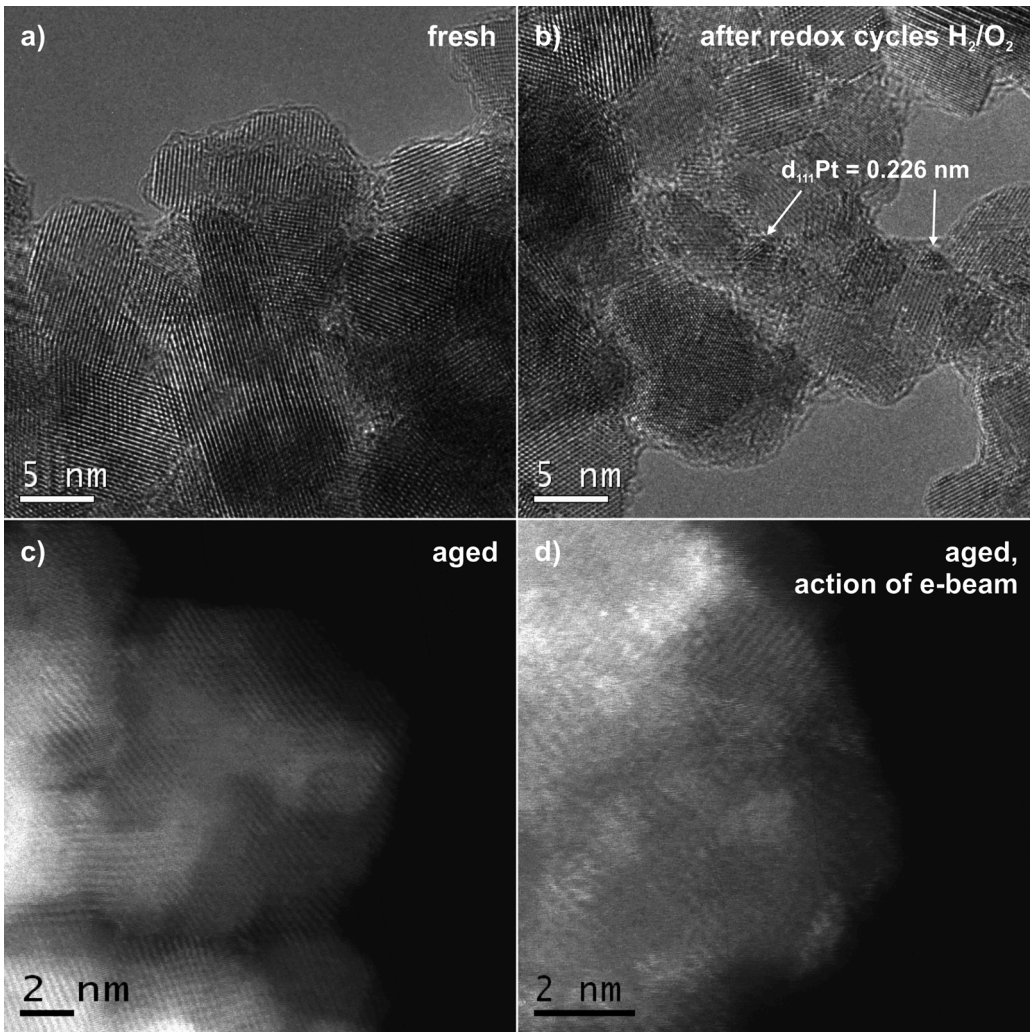

Fig. 3. (a) – (b) HRTEM and (c) – (d) HAADF-STEM images of 8Pt/CeO_2 catalyst: a) fresh; b) after redox cycles: TPR-H_2 (10 vol.%H_2, -40 – 450 °C, 10 °C/min) and TPO (10 vol.%O_2, -40 – 450 °C, 10 °C/min) c) aged (exposed to air for a year); d) aged (exposed to air for a year), the image acquired after exposure of the catalyst to electron beam for several minutes. In b) and d) images small Pt clusters are observed.

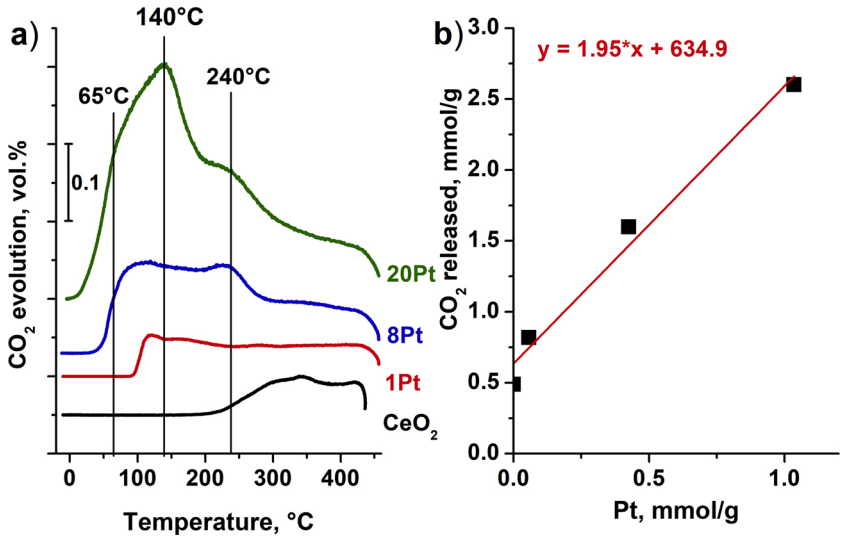

Fig. 4. (a) Temperature dependences of the CO_2 evolution for 1Pt/CeO_2, 8Pt/CeO_2, 20PtCeO_2 and pure CeO_2 samples during TPR-CO. All TPR curves except that of pure CeO_2 are shifted up for clarity. (b) Dependence on the Pt loading of the amount of oxygen evolved from the catalysts measured by CO_2 evolution. The slope of the line is close to 2.

1Pt/CeO_2 catalyst, there is an isolated peak (γ) with the maximum near 150 °C, which corresponds to the hydrogenation of O atoms near Pt^{2+} single-atom species [28,39,93]. An increase in the Pt content up to 8 wt % leads to the appearance of an additional peak (β) at lower temperatures (~90 °C) and to a decrease in the temperature of the γ peak maximum for to ~110 °C. In addition, for this catalyst H_2 consumption begins already below 50 °C. For the 20Pt/CeO_2 catalyst, a further decrease in the reduction temperature to 20 °C is observed (peak α) with a slightly lower reduction temperature for peak γ (Pt^{2+}-SA). Peak α for the 20 %Pt catalyst is very narrow (half-width of ~ 5 °C), indicating a high efficiency of hydrogen interaction with the oxygen of highly loaded Pt/CeO_2 catalysts. Peaks at temperatures between -80 °C and 20 °C can be assigned to the reduction of PtO_x clusters [104], and the small peak width is indicative of a uniform PtO_x particle size distribution [104]. This suggests that there is a high abundance of PtO_x in the 20 %Pt catalysts, and that a small fraction of the Pt in the 8 %Pt catalyst is also in the form of PtO_x clusters.

3.5. TPR-CO data: Correlation with ex situ XPS data

A series of XPS Pt4f spectra (see Fig. 5a) was obtained *ex situ* after step-by-step treatments of the 20Pt/CeO_2 sample in the atmosphere of CO at different temperatures as described in Section 2.2. These XPS experiments allow correlating the temperature range of generation of mobile reactive oxygen (oxygen release) in TPR-CO with the oxidation states of Pt and Ce. The Pt4f spectra reveal three states: $Pt^{\delta+}$, Pt^{2+} and Pt^{4+}. The state with the lowest binding energy in Fig. 5a is denoted as $Pt^{\delta+}$, as the value of $E_b(Pt4f_{7/2})$ =71.5 eV indicates a platinum to ceria electron transfer resulting in a slightly positive charge δ+ of platinum atoms in metallic particles [17,105–107].

Fig. 5b shows the dependence of relative concentrations (atomic ratio of Pt^{n+} to Pt_{total} in the sample) of ionic and metallic states of Pt obtained from the curve fitting analysis of the Pt4f spectra. According to Fig. 5a the catalyst treated at room temperature contains only oxidized platinum as Pt^{2+} and Pt^{4+} ions. Increasing treatment temperature does not lead to significant changes in the state of Pt up to 100 °C. However, at 150–250 °C complete conversion of Pt^{4+} takes place with the appearance of reduced $Pt^{\delta+}$, while the concentration of Pt^{2+} ions remains essentially unchanged. The temperature increase from 250 to 450 °C causes a decrease in concentration of Pt^{2+} and growth of reduced platinum $Pt^{\delta+}$. Ce^{3+} concentration practically does not change up to 150 °C, while there is a sharp increase in the ratio of Ce^{3+}/Ce from 0.12 at 150 °C to 0.27 at 200 °C indicating a relation between Pt^{4+}, Ce^{3+} and reactive oxygen (Figs. 5, S6 and Table S2). The constant Ce^{3+}/Ce ratio at the surface below 150 °C in absence of O_2 in the reactant gas-flow suggests faster bulk to surface migration of O atoms than the removal of surface O atoms by CO. This maintains a steady concentration of oxygen (and the corresponding Ce^{3+}/Ce ratio) at near-surface regions. The sustained CO_2 evolution during TPR-CO (Fig. 4a) in the temperature range 0–200 °C supports this explanation.

According to the XPS data (Fig. 5), oxygen release from the sample is not accompanied by the reduction of cationic platinum at temperatures <100 °C. Since these measurements are performed *ex-situ*, we cannot completely discard dynamic changes in the oxidation states of the cationic Pt species under reaction conditions. Nevertheless, comparison of the TPR-CO and XPS data shows that the most intensive CO_2 formation (oxygen release) occurs below 200 °C in the presence of Pt^{2+} and Pt^{4+} ions. Results of our DFT calculations described in the following relate the interplay of Pt^{2+} and Pt^{4+} ions in inner regions of ceria nanoparticles with the facilitated generation of reactive oxygen species.

3.6. DFT data

The role of surface Pt^{2+} species [32] and metallic Pt [108] during CO oxidation is relatively well-understood: Pt^{2+} ions can facilitate formation of oxygen vacancies (O_v) and oxygen diffusion in CeO_2 [109–111], whereas metallic Pt provides sites for favorable CO adsorption [47,112]. Yet, the origin, stability and function of Pt^{4+} ions spectroscopically detected in ceria ([25,69,91] and references therein) are less clear. Introduction of Pt^{4+} cations in crystalline positions of notably larger Ce^{4+} cations causes strong displacements of the surrounding oxygen anions [113]. Atomic Pt dopants preferably occupy surface positions on ceria, where they are unstable in the Pt^{4+} state and readily converted to Pt^{2+} *via* O_v formation [22,110]. Interestingly, a previous DFT modelling study indicated that Pt^{4+} dopants are also unstable in cationic positions of ceria bulk with respect to reduction to Pt^{2+} and spontaneous release of

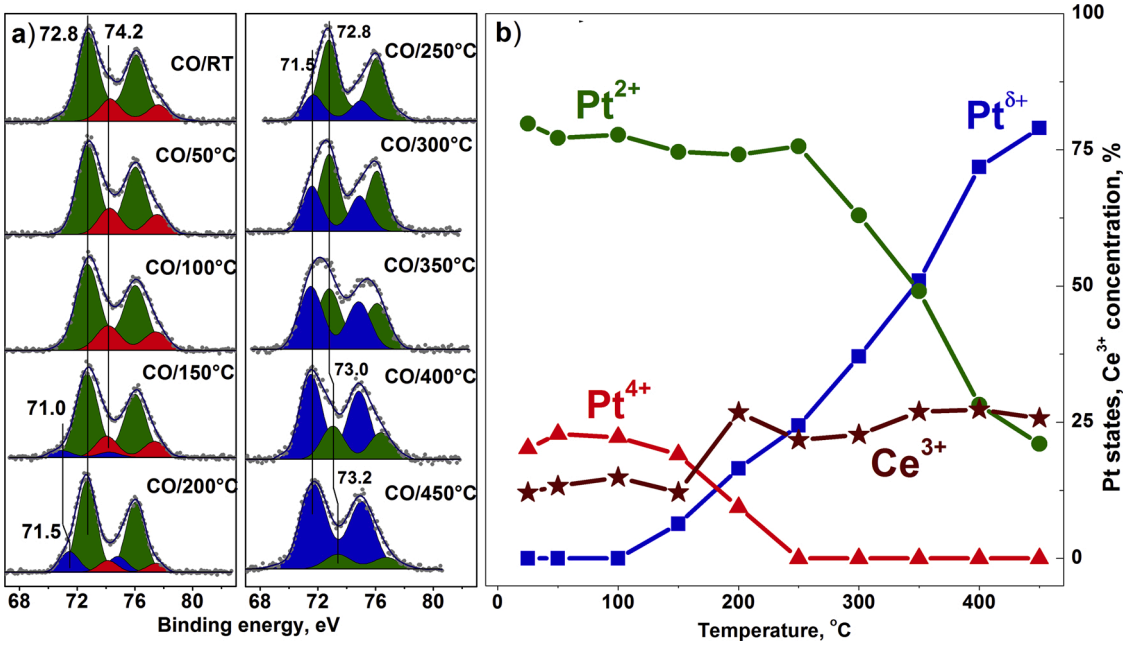

Fig. 5. (a) *Ex-situ* XPS Pt4f spectra obtained after treatment of the 20Pt/CeO_2 sample with CO during stepwise reduction from 25 °C to 450 °C. Curve fitting was performed after background subtraction; (b) Dependence of the relative concentrations of Pt (Pt^{n+}/Pt_{total}) and Ce^{3+} (Ce^{3+}/Ce_{total}) species in the 20Pt/CeO_2 sample on temperature of the treatment in CO derived from the XPS spectra.

a charge-compensating vacancy O_v [113]. Therefore, important questions are (*i*) how stable are Pt^{4+} dopants in cationic positions of ceria and (*ii*) how do Pt^{4+} species affect the propensity of Pt/CeO_2 samples to release O atoms, which serves as an oxidation-activity descriptor. To this end, we performed density functional calculations using models of Pt-doped ceria in bulk and nanoparticle forms and investigated the formation of O vacancies therein.

Bulk models (Fig. 6a) represent inner regions of big Pt/CeO_2 particles distant from the particle surface. The substitution of a lattice Ce^{4+} with Pt^{4+} distorts cubic coordination environment (Ce-O(×8) = 237 pm) of Ce^{4+} centres to characteristic octahedral coordination (Pt-O(×6) = 210 pm and Pt-O(×2) = 294 pm) of d^6 metal centres [114]. This distortion displaces two (of the nearest eight) O atoms by 84 pm away from Pt, thus weakening their binding with the lattice [113,115]. The resulting 6 + 2O coordination of Pt^{4+} is stabilized by 164 kJ/mol over the cubic coordination with Pt-O(×8) = 229 pm, which appeared to be a local minimum in the structure optimization process started from Pt^{4+} cation in the Ce^{4+} site featuring the undistorted cubic oxygen coordination. In

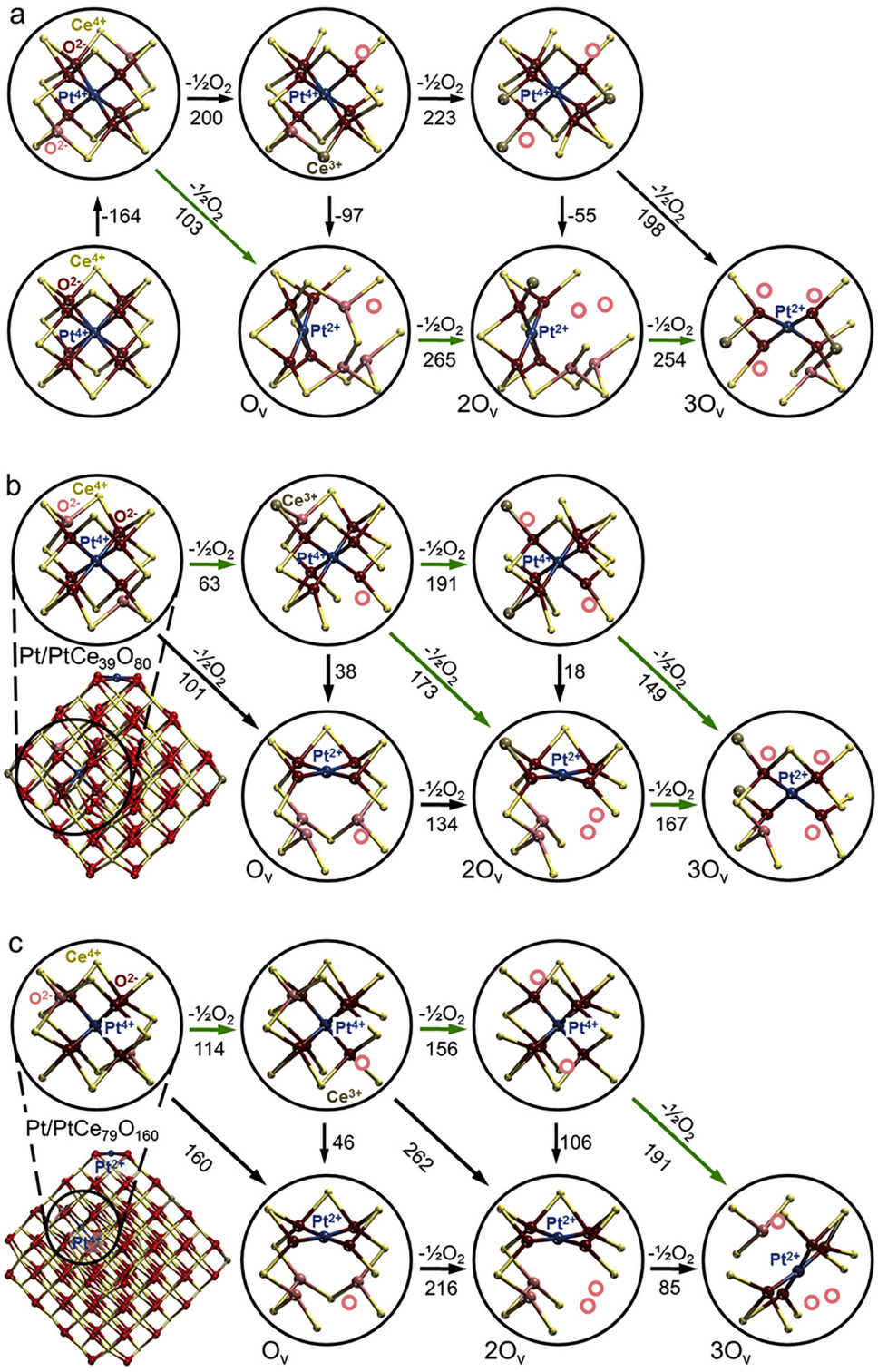

Fig. 6. Oxygen vacancy (O_v) formation energies in kJ/mol near Pt dopants in ceria bulk and nanoparticles. (a) Bulk model $PtCe_{31}O_{64-n}$ (n = 0, 1, 2, 3) with one Pt atom substituting a Ce atom. (b), (c) Model particles $Pt/PtCe_{39}O_{80-n}$ and $Pt/PtCe_{79}O_{160-n}$, respectively, with the first Pt atom bound in the 2+ state to a {100} nanofacet and the second Pt atom located in a Ce site inside the particle. O atoms and the corresponding O_v positions more distant from the interior Pt dopant are shown as pink balls and circles. Positive energy values indicate destabilization. Green arrows indicate most energetically favored channels of formation up to three O_v near each Pt dopant. (For interpretation of the references to colour in this figure legend, the reader is referred to the web version of this article.)

contrast to the aforementioned DFT result [113], in our calculations the most energetically favorable O_v creation near the Pt^{4+} dopant in bulk ceria by removing an O atom 294 pm away from the dopant is not spontaneous and still requires energy, even if it is much less than E_{Ov} =321 kJ/mol we calculated for undoped bulk ceria.

To further evaluate the stability of the dopant Pt, we have calculated the doping energy E_{dop} for Pt-doped systems under study. E_{dop} defines the energy required or gained when replacing a Pt atom for a Ce atom, i. e. the energy of the reaction:

$$Pt_bCe_aO_{2a} + Pt + (2\text{-}n)/2\ O_2 \rightarrow Pt_{b+1}Ce_{a-1}O2_{a-n} + CeO_2,$$

where $Pt_bCe_aO_{2a}$ and $Pt_{b+1}Ce_{a-1}O2_{a-n}$ are the models before and after doping, respectively, b, a and n correspond to the number (per supercell) of Pt atoms and Ce atoms in the undoped system and O vacancies in the doped system, respectively. The reference systems used to represent atomic Pt dopant, O_2, and CeO_2 are a Pt_{79} nanoparticle, gas-phase O_2, and bulk CeO_2. E_{dop} is therefore calculated as:

$$E_{dop} = E[PtCe_{a-1}O2_{a-n}] + E[CeO_2] - E[Ce_aO_{2a}] - E[Pt_{79}]/79 - (2\text{-}n)\ E[O_2]/2.$$

The resulting E_{dop} for bulk ceria and for $PtCe_{40}O_{80}$, and $PtCe_{80}O_{160}$ nanoparticles are −43, −123 and −101 kJ/mol, respectively. This indicates that doping is a thermodynamically favorable process in all cases studied, and that it is more favorable for ceria nanoparticles than for bulk ceria. There is also a slight size effect – doping with Pt is somewhat less favorable in the larger particle, which is consistent with its closer similarity to the bulk ceria system.

Furthermore, we have inspected whether the states with Pt^{4+} in ceria bulk positions are stable with respect to their reduced counterparts under different conditions. To do so, we have calculated the evolution of Gibbs free energy with changing chemical potential (see Fig. S7) using a simple *ab initio* thermodynamics model [116]. The resulting free energy plots indicate that the states with Pt^{4+} are the most thermodynamically stable under relevant gas-phase chemical potentials. In addition, and not surprisingly, the Gibbs free energy differences between states with and without vacancies become smaller for lower (more reducing) chemical potentials. This indicates that the resulting oxygen vacancy formation Gibbs free energies are smaller than the oxygen vacancy formation internal energies. Note that oxygen vacancy formation energies calculated with the DFT + U approach are quite sensitive to the choice of U parameter. It is therefore more cautious to focus on qualitative trends instead of absolute values of the calculated energy differences. In this regard, we emphasize that the presence of Pt dopants significantly facilitates the formation of oxygen vacancies in inner positions of ceria nanoparticles, and that the substitution of Pt for Ce is exothermic and more favorable for ceria nanoparticles than for bulk ceria.

The present calculated energies strongly suggest that the exothermic O_v formation energy reported in [113] for Pt-doped bulk ceria probably resulted from using the octahedral 8 O coordination configuration of Pt^{4+} as a reference instead of 164 kJ/mol more stable 6 + 2 O coordinated configuration. O_v creation leaves behind two electrons reducing either two Ce^{4+} to Ce^{3+} or the Pt^{4+} cation to Pt^{2+}, leading to significantly different energies and structures. When Pt^{4+} is reduced, the formed Pt^{2+} cation acquires a square-planar coordination by four O^{2-} and the corresponding E_{Ov} is 103 kJ/mol (for Pt-doped bulk ceria). When two Ce^{4+} are reduced instead, E_{Ov} increases to 200 kJ/mol and Pt^{4+} remains in the octahedral coordination with a 6 + 1 oxygen environment. Hence, Pt^{4+} dopants in bulk CeO_2 tend to be reduced to Pt^{2+} already at the onset of O release due to the limited reducibility of bulk Ce^{4+} cations. The standard enthalpy of the reaction $CO(g) + ½O_2(g) = CO_2(g)$, $\Delta H = -283$ kJ/mol [117], estimates very roughly how endothermic the vacancy formation process $Pt/CeO_2 = Pt/CeO_{2-x} + ½O_2(g)$ can be for these coupled reactions to remain thermodynamically feasible. The calculated formation energies of the first, second and third O_v near a Pt dopant in bulk ceria are within this estimate and the E_{Ov} values become lower for more reduced doped nanoparticles considered in the following.

Nanoparticle models of two sizes, 1.4 nm $Pt/PtCe_{39}O_{80}$ (Fig. 6b) and 1.9 nm $Pt/PtCe_{79}O_{160}$ (Fig. 6c), were chosen to explore the surface and near-surface reactivity of nanocomposite Pt/CeO_2. The respective E_{Ov} energies calculated for the NPs (Fig. 6b, c) differ both quantitatively and qualitatively from the data for Pt/CeO_2 bulk (Fig. 6a). Again (see Fig. 6b), creating the first O_v at a Pt^{4+} centre inside the NP can have the same two outcomes depending on the type of species reduced. Here, however, reducing two Ce^{4+} instead of the Pt^{4+} gives a very low value E_{Ov} =63 kJ/mol, being in the NP 137 kJ/mol smaller than in the bulk. This is due to higher reducibility of low-coordinated surface Ce^{4+} ions of NPs [78] making O_v formation less endothermic than when Pt^{4+} is reduced to Pt^{2+}. Differently from bulk, Pt^{4+} dopants in ceria particles can withstand the formation of even the second O_v around them without being reduced to Pt^{2+} (E_{Ov} values are similar for forming Pt^{2+} and 2 Ce^{3+} in the $Pt/PtCe_{39}O_{80}$ model, while the reduction of 2 Ce^{4+} is clearly favored for the larger $Pt/PtCe_{79}O_{160}$ NP). The formation of the third O_v around the Pt cation in the nanoparticles requires significantly less energy than in bulk ceria. Qualitatively similar results to those just described for the $Pt/PtCe_{39}O_{80}$ particle are obtained for larger $Pt/PtCe_{79}O_{160}$ NP model (Fig. 6c).

These findings unveil the promoting effect of Pt^{4+} species on the oxidative capacity measured for nanoparticulate Pt/CeO_2 samples with high Pt content. They also clarify the discrepancy between the instability of Pt^{4+} predicted by previous DFT calculations [113] using bulk ceria as host oxide model and the prevalence of Pt^{4+} species identified experimentally studies of Pt-doped ceria.

3.7. TPR CO + O_2: catalytic data

Fig. 7 illustrates catalytic properties of the Pt/CeO_2 samples. For the $1Pt/CeO_2$ sample (Fig. 7a), the CO conversion curves during heating and cooling have a characteristic S-shape and almost coincide, reflecting stability of the active centers. The catalyst starts to be active above 150 °C, with T_{10} = 175 °C and T_{50} = 230 °C. This is in good agreement with the literature data for Pt/CeO_2 catalysts featuring atomically dispersed Pt^{2+} species [32,34,103,118]. The second heating of this sample leads to an almost identical curve.

Behavior of the $8Pt/CeO_2$ sample (Fig. 7b) is significantly different from that of $1Pt/CeO_2$ one. During the first heating, the catalyst is active already below room temperature and T_{10} and T_{50} are 18 and 55 °C, respectively. During cooling, the CO conversion decreases very mildly, reaching 65 % at -10 °C. During the second heating, from −10 °C to 100 °C the CO conversion rises slowly to ~75 % and after heating above 100 °C rapidly reaches 100 %.

In turn, the as-prepared $20Pt/CeO_2$ catalyst (Fig. 7c) is also active during the first heating cycle already below room temperature, with T_{10} = 10 °C and T_{50} = 35 °C. During cooling, the CO conversion remains almost constant down to below room temperature and decreases just slightly to 95 % at −10 °C. During the second heating, the 95 % CO conversion is maintained and increased to 100 % at 120 °C, with just a slight decrease between 50 °C and 75 °C. The conversion values observed during the second heating coincide with those obtained after preliminary treatments of the sample directly in the reactor in gas mixture of 20 % O_2 in helium at 450 °C (Fig. 7d) showing 100 % CO conversion already at -10 °C. The lower CO conversion for the $8Pt/CeO_2$ and $20Pt/CeO_2$ catalysts during the first heating is therefore probably due to significant amount of water in the initial catalyst at low temperatures.

In order to further validate this assumption, we collected XPS O1s spectra of the as-prepared samples prior to the first heating cycle and analyzed the outlet gas-mixture composition during the heating and cooling cycles. The decomposition of O1s spectra of the Pt/CeO_2 catalysts (Fig. S8) results in three peaks with E_b(O1s) = ~529.6, ~531.6 and ~533.6 eV attributed to ceria lattice oxygen, oxygen defects including OH-groups and adsorbed H_2O/CO_x species, respectively. H_2O is released

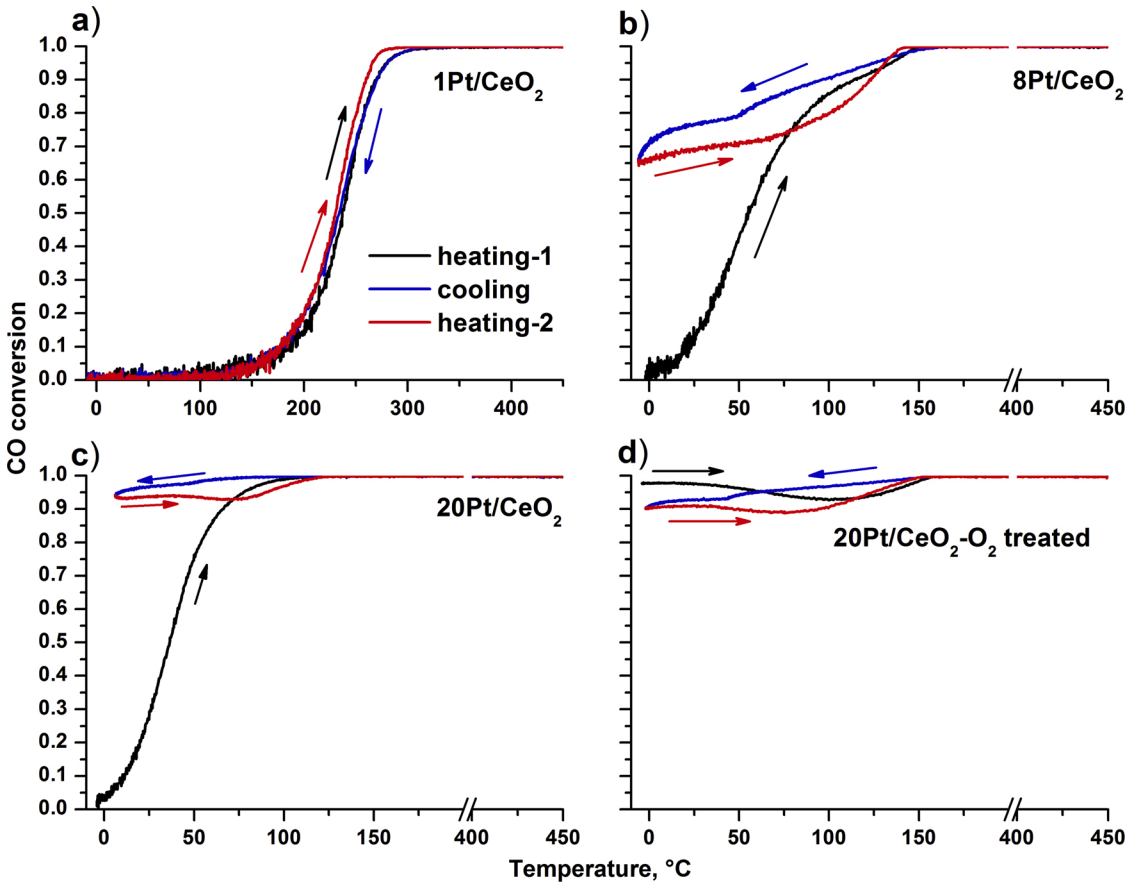

Fig. 7. Temperature dependencies of CO conversion for the catalysts 1Pt/CeO_2 (a), 8Pt/CeO_2 (b), 20Pt/CeO_2 (c) and 20Pt/CeO_2 treated in O_2 (d) obtained in the TPR-CO + O_2 regime during repetitive heating/cooling cycles (first heating, cooling, second heating) in the reaction mixture. 20Pt/CeO_2-O_2 is the catalyst priory treated in O_2 at 450°C directly in the reactor.

from OH-groups and adsorbed water during the first samples heating in the reaction mixture, as illustrated in Fig. S9 for the 8Pt catalyst. Water removal from the catalyst during heating in the reaction mixture unblocks active sites and thus increases activity maintained during the subsequent cooling and heating. After cooling in the reaction mixture the activity remains the same as shown in Fig. 7b–d. Data in Fig. 7 evidence the reversibility of catalysts activity during the heating/cooling runs and the absence of inhibition by water. The initial and spent catalysts were further studied in order to examine reversibility of the high catalytic activity and blocking active sites by water (Fig. S9d,e). These investigations showed highly reproducible catalytic activity under conditions of repetitive heating/cooling cycles. Addition of water vapor in the reaction mixture to explicitly block active sites caused disappearance of the activity in the temperature range below 60−70 °C (Fig. S9f), further confirming that the initial inactivity of the catalyst at these temperatures was due to the presence of adsorbed water.

Comparison of XPS data for the 1Pt/CeO_2, 8Pt/CeO_2 and 20Pt/CeO_2 samples before and after CO + O_2 reaction shows that the reaction medium does not permanently modify composition of the catalyst (Fig. S10). The ratio between different forms of platinum does not change significantly for the 1 % and 8 %Pt catalysts, with only a small fraction of Pt^{4+} being converted to Pt^{2+} in the later. The spectra for the 20 %Pt catalysts do indicate a slight increase in the concentration of metallic Pt and a decrease in the concentration of Pt^{4+}. We attribute this to the reduction of unstable Pt^{4+} species in the highly loaded samples, which indeed suggests that a small fraction (less than 10 %) of the ionic Pt in the 20Pt/CeO_2 catalyst will not survive in ionic form after reaction. However, and as shown below, the presence of a small fraction of Pt^0 species does not have a significant effect on the catalytic properties of the 20Pt/CeO_2 sample at low temperatures. This is demonstrated by the similarity to the catalytic properties of the 8Pt/CeO_2 sample, in which we do not find any Pt^0, strongly suggesting that the observed low-temperature CO oxidation is not triggered by metallic Pt.

To quantitatively compare the catalytic activity of all samples, 8Pt/CeO_2 and 20Pt/CeO_2 samples were diluted with CeO_2 powder (the resulting catalysts are hereafter denoted with an †), so that the amount of Pt in these samples was made the same as in the 1Pt/CeO_2 sample. Specific reaction rates (W) (Fig. S11) and turnover frequencies (TOFs) per catalytic center (Fig. 8b) were derived from the TPR-CO + O_2 data shown in Fig. 8a as described in the Supplementary Materials (SM).

Fig. 8a shows low-temperature activity of the diluted samples 8Pt/CeO_2† and 20Pt/CeO_2†. These curves are very similar, and for both of them the conversion of CO begins significantly below 0 °C, with T_{10} and T_{50} ca. 10 °C and 115 °C, respectively. Most importantly, the activity of these catalysts (with nominally 1 wt%Pt) is much higher than that of the 1Pt/CeO_2 sample. For the diluted catalysts, the full conversion is achieved at ~150 °C, while the 1Pt/CeO_2 catalyst is still practically inactive at this temperature. These diluted catalysts active well below room temperature show significantly lower light-off temperatures than previously studied Pt/ceria catalysts [7,21,32,34,39,40,46,56,58,103,118–120]. Such low-temperature activity has been so far reported only for catalysts based on Au or Co_3O_4 [121–126]. The activation energy in the interval from -50 °C to 50 °C is 9 kJ/mol for both 8Pt/CeO_2† and 20Pt/CeO_2† samples, i.e. much lower than 50.7 kJ/mol found for the 1Pt/CeO_2 catalyst at T ≥ 150 °C (Fig. S11). Such low activation energies may indicate that the exothermic reaction leads to local heating of the catalyst bed or that mass transport resistances play a role. However, the absence of heat transfer was confirmed by Mears' criterion and the

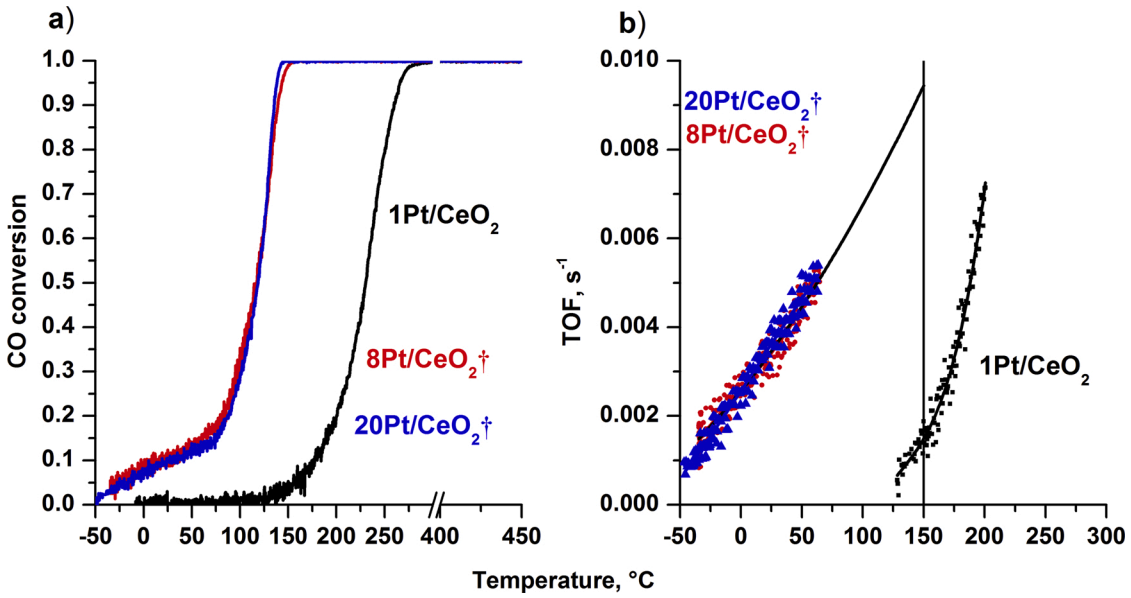

Fig. 8. (a) Temperature dependencies of CO conversion and (b) TOF temperature dependencies for the catalyst 1Pt/CeO_2 and diluted 8Pt/CeO_2† and 20Pt/CeO_2† ones. The dilution was performed as follows: the catalyst 8Pt/CeO_2 was diluted with CeO_2 by 8 times, 1/8 × 8Pt/CeO_2+ 7/8 × CeO_2, and 20 Pt/CeO_2 one – by 20 times, 1/20 × 20 Pt/CeO_2+19/20 × CeO_2.

calculated adiabatic heating in the range -30 ÷ +73 °C does not exceed 4.6 °C (see SM for details). With respect to mass transfer limitation, external diffusion limitations were discarded by comparing the concentration of CO in the gas film over the surface of the catalyst with that in the gas phase, and internal diffusion limitations were discarded on the basis of the Weisz criterion.

The much lower activity and higher activation energy of the 1Pt/CeO_2 catalyst compared to the diluted 8Pt/CeO_2† and 20Pt/CeO_2† catalysts indicates that the undiluted 8Pt/CeO_2 and 20Pt/CeO_2 catalysts are more active than the 1Pt/CeO_2 catalyst not only due to higher Pt loading, but also because of the presence of different sites that are more active at low temperatures. A very close resemblance of the temperature dependencies of CO conversion for the diluted 8Pt/CeO_2† and 20Pt/CeO_2† catalysts indicates that different activities of the undiluted counterparts can be attributed mostly to different amount of active centers.

When comparing TOF values from different studies one should take into account experimental conditions at which such studies were performed. The present high activity for the 8Pt/CeO_2 and 20Pt/CeO_2 catalysts (TOF = 0.0035 s^{-1} at 25 °C) is similar to that reported by Gatla et al. [103] for 2.5 wt%Pt/CeO_2 catalyst (TOF = 0.003 s^{-1} at 25 °C). Very high activity was also reported by Liu and coauthors [39] for 10 wt %Pt/CeO_2 catalyst (TOF = 0.0763 s^{-1} or 0.006 s^{-1} at 40 °C when normalizing by the amount of surface Pt (0.15) or the total amount of Pt in the catalyst, respectively). These TOF values are similar to those obtained by us for the 8Pt/CeO_2 and 20Pt/CeO_2 catalysts (TOFs = 0.0043 and 0.0041 s^{-1} at 40 °C, respectively, again normalized by the total amount of Pt). We should also note different reaction conditions in these studies, precluding their direct one-to-one comparison. Notwithstanding, TOF data obtained in our work are very close to published data at 25 °C or higher temperatures [39,103]. However, we also report data obtained at temperatures below 0 °C, with correspondingly high values of TOF = 0.0016 s^{-1} at −30 °C for the 8Pt/CeO_2 and 20Pt/CeO_2 catalysts. The articles by Liu et al. [39] and Wang et al. [56] do not report activity at these low temperatures, but it can be estimated by extrapolating the TOF values at T = 40−50 °C. The resulting TOF values at T = −30 °C are shown in Table S3, revealing that the catalyst prepared by Wang et al. [56] would have an extrapolated TOF = 0.0045 s^{-1} comparable to the TOF we report at the same temperature (0.0016 s^{-1}). However, no direct experimental measurements below 0 °C were performed in that work, where the active catalytic sites were proposed to be in PtO_x clusters [56]. Similarity of our kinetic data to those by Wang et al. suggests the same origin of the active sites in our catalysts, i.e. PtO_x clusters. The presence of such PtO_x clusters in our samples is further supported by the similarities between TPR-CO and TPR-H_2 spectra shown for the 20Pt/CeO_2 catalyst and those obtained by Ke et al. for PtO_x clusters supported on ceria nanowires [45]. To shed more light on the nature of the active sites in the catalysts with high Pt content mediating the observed low-temperature activity, our catalysts were further studied by TPR-CO at the same conditions as in the TPR-CO + O_2 experiments but without O_2 in the feed.

3.8. Comparison of TPR-CO and TPR-CO + O_2

According to the TPR-CO data in Fig. 4, mobile reactive oxygen is generated below room temperature in the 8Pt/CeO_2 and 20Pt/CeO_2 catalysts. To assess whether this reactive oxygen originated from the CeO_2 lattice in the presence of Pt^{2+} and Pt^{4+} ions can provide a stationary CO oxidation reaction rate below room temperature (at least until all available lattice O is depleted), we compared these TPR-CO results with the results of TPR experiments performed with both CO and O_2 present in the gas mixture (TPR-CO + O_2) (Figs. 9, 10, S12).

CO_2 evolution during temperature programmed heating in CO ambient in the presence of gas-phase O_2 (TPR-CO + O_2) and in its absence (TPR-CO) for the 20Pt/CeO_2 catalyst is shown in Fig. 9a. The catalyst was pretreated in the 20 %O_2/He atmosphere at 450 °C for 2 h to remove adsorbed water and other impurities, and the reaction mixture was inlet to the catalyst cooled to −40 °C with continued cooling of the reactor. The substantially higher TPR-CO + O_2 conversion to CO_2 at room temperature and below than for TPR-CO demonstrates the direct participation of gas-phase oxygen in the CO oxidation. Lower TPR-CO + O_2 conversion values in this temperature range at lower switch-on O_2 pressure (not shown) also supports this result. For a quantitative comparison in Fig. 9b the dependences of the specific reaction rate (W) on temperature are presented on a logarithmic scale. They show several orders of magnitude difference in the reaction rates. We compared data obtained with the diluted and undiluted catalyst (20Pt/CeO_2† and 20Pt/CeO_2) for the TPR-CO + O_2 (Fig. 8) and TPR-CO (Fig. 9) rates, respectively. The diluted catalyst 20Pt/CeO_2† was used because CO conversion in the TPR-CO + O_2 experiment for the undiluted

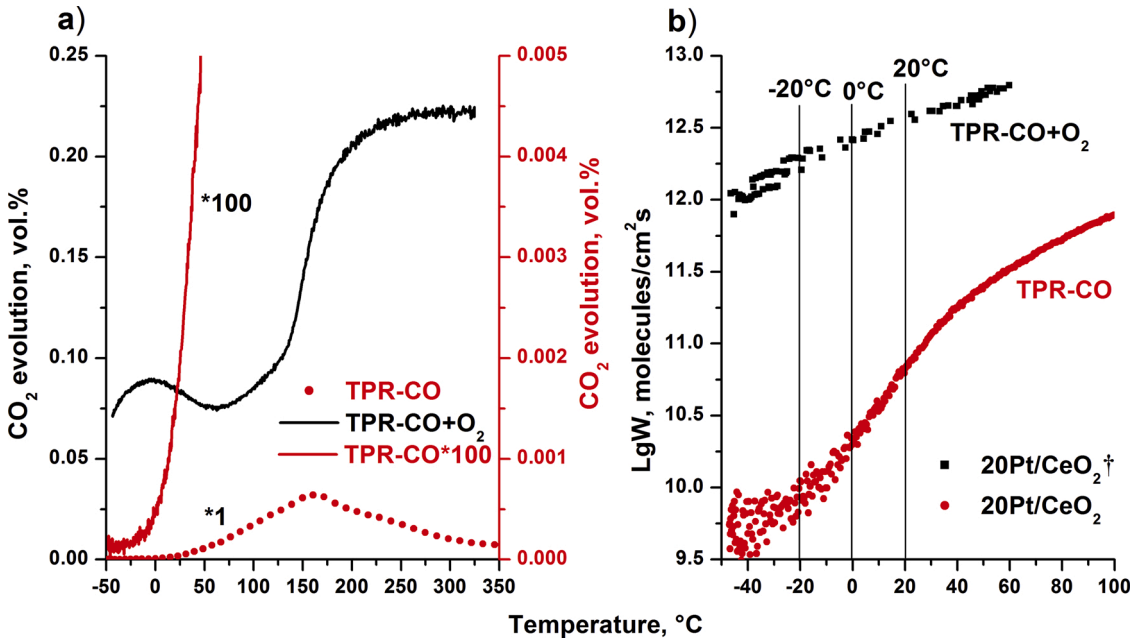

Fig. 9. (a) Temperature dependence of CO_2 evolution (concentration) during TPR-CO and TPR-CO + O_2 for the 20Pt/CeO_2 catalyst at the same CO pressure. In order to underline small contribution of TPR-CO *vs* TPR-CO + O_2, 100 times amplified CO_2 evolution data during TPR-CO are also presented (cf. the right-hand axis). The experimental conditions were as follows: CO – 0.2 vol.%, O_2 – 0 (TPR-CO), 1.0 vol.% (TPR-CO + O_2), catalyst weight 0.1 g, flow of reaction mixture 1000 cm^3/min, heating rate – 10 °C/min. (b) Temperature dependences of the specific CO oxidation reaction rate W calculated for the 20Pt/CeO_2 catalyst from the kinetic data of TPR-CO + O_2 and TPR-CO. The TPR-CO + O_2 rate for the 20Pt/CeO_2† catalyst was calculated with the aid of the CeO_2 dilution method (see SM).

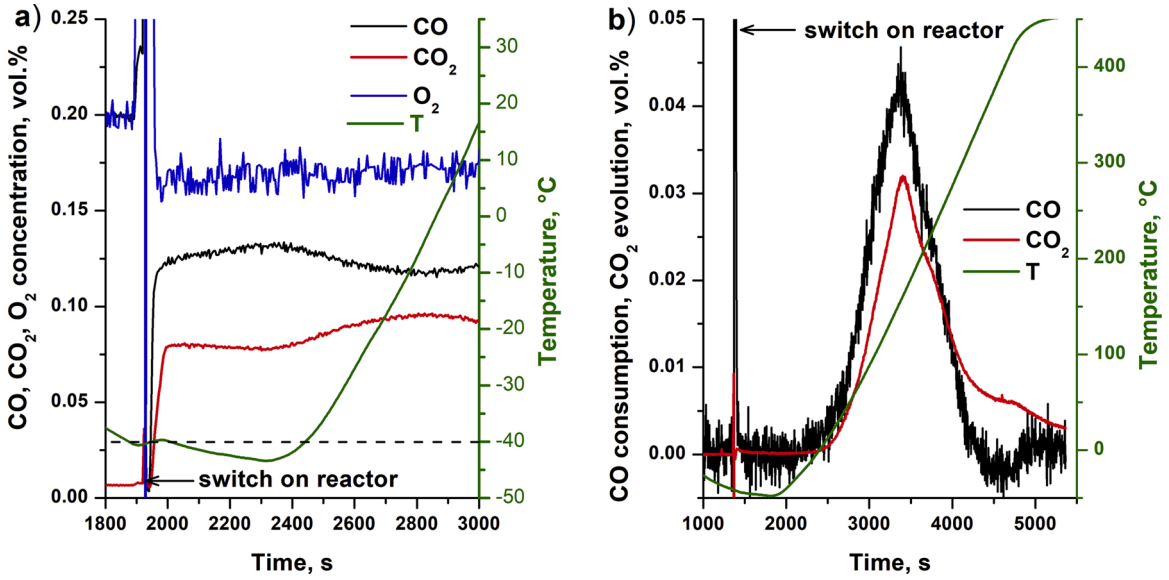

Fig. 10. Admission of the reaction mixture onto the catalyst 20Pt/CeO_2 cooled to -40 °C during (a) TPR-CO + O_2 and (b) TPR-CO. For clarity, the concentration scale of O_2 is shifted down by 0.8 vol.%, because O_2 concentration is much higher than CO and CO_2 concentrations.

catalyst was too high (>90 %) for determining the reaction rate. The undiluted catalyst 20Pt/CeO_2 was used because CO_2 evolution in the TPR-CO experiment for the diluted catalysts was very low. This dilution should however not affect the specific reaction rates, since the two catalysts have the same type of active sites but in different amounts. The resulting specific rates for TPR-CO + O_2 are 54, 118 and 224 times higher at 20, 0 and -20 °C, respectively, than those determined from TPR-CO. From the Arrhenius dependences of the CO oxidation rate for TPR-CO and TPR-CO + O_2 (Fig. S12), the activation energies were calculated to be 40.0 and 9 kJ/mol, respectively, thereby directly evidencing different reaction pathways of the oxidative CO interaction with oxygen of the catalyst and oxygen of the gas phase.

In order to further asses the activity of these catalysts at very low temperatures, we focus on the CO conversion upon admission of the reaction mixture on pre-oxidized 20Pt/CeO_2 catalyst at −40 °C. Fig. 10 demonstrates a sharply different behavior upon admission of CO + O_2 or of only CO. With O_2 present in the gas phase, CO oxidation begins already at −40 °C (Fig. 10a), while without O_2 it only begins at −3 °C (Fig. 10b). Noteworthy, concentrations of CO and O_2 immediately decrease upon admission of reactant flow with simultaneous increase of CO_2 concentration, reaching the stationary conversion of about 40 % at −40 °C. The fast observed response of CO_2 formation indicates absence

of CO_2 desorption limitations at low temperatures.

Thus, the experimental data presented above show that CO oxidation at low temperatures is not an efficient process without presence of gas-phase oxygen. In other words, the mobile oxygen contained in the catalyst alone does not provide high CO conversion at low temperature. The activated oxygen from the gas phase mediates the low-temperature CO oxidation activity of the Pt/CeO_2 catalysts with high Pt loading.

3.9. The effect of O_2 flow interruption

In order to better understand the role of gas-phase oxygen at low reaction temperatures O_2 gas supply interruption effects during the low-temperature oxidation of CO were studied. The same pretreatment as described in the previous section was applied to remove adsorbed water from the $20Pt/CeO_2$ catalyst, which did not affect the structure and oxidation state of the latter. The catalyst was subsequently cooled in the reaction mixture to ~33 °C, at which a stationary catalytic state was observed with a constant CO conversion. Oxygen supply to the catalyst in this stationary state was then repeatedly turned off and on in 250 s intervals.

Fig. 11a shows evolution of CO, CO_2 and O_2 concentrations with time during periods with and without oxygen in the gas phase; Fig. 11b displays the same data for CO and CO_2, together with the catalyst temperature. Switching-off the supply of O_2 was accompanied by fast CO_2 concentration decrease, CO concentration increase and temperature decrease in the reactor. The sharp increase of CO_2 concentration occurring after switching-on the O_2 flow indicates that essentially all CO is oxidized by oxygen from the gas phase rather than by lattice oxygen. Switching-on O_2 flow also caused a slight increase of reactor temperature correlating with formation of CO_2.

The fast response to the interruption of O_2 supply evidences a direct participation of gas-phase oxygen in the low-temperature oxidation of CO, while ceria lattice oxygen reacts with CO much more slowly at these conditions.

4. Discussion

4.1. CO oxidation at temperatures below 100 °C

Investigation of Pt/CeO_2 samples synthesized by co-precipitation and calcined at 600 °C revealed strong dependence of their oxidative catalytic activity on the Pt content. At 1 wt% of Pt, the CO + O_2 reaction starts at T > 120 °C and the catalyst exhibits a very high stability and reversibility in the temperature-cyclic activity measurements. Compared with the purely CeO_2 catalyst the onset of CO oxidation is shifted from T_{50} = 350 °C to T_{50} = 235 °C, i.e. the light-off curve is shifted to ca. 115 °C lower temperature (Figs. 7, S13). We assign this effect to the appearance of single-atom Pt^{2+} species accompanied by local restructuring of ceria surface and formation of less strongly bonded oxygen centres around Pt^{2+} ions. This agrees with the interpretations by Datye and co-authors [31,32,118] and Ye et al. [120] who related the CO oxidation enhancement with the action of single-atom sites Pt^{2+}.

When platinum loading increases to 8 wt%, our Pt/CeO_2 catalyst acquires new remarkable properties, namely, its oxidative activity extends to as low temperature as –50 °C. This effect, as shown by our experiments with catalysts dilution by pure CeO_2, is not due to merely increased number of the single-atom Pt^{2+} sites at increased platinum loading. The appearance of such low-temperature oxidation of CO at this higher Pt loading strongly suggests generation of new considerably more active sites and realization of new reaction pathways. The $20Pt/CeO_2$ catalyst with even higher Pt loading converts CO in the first testing cycle starting from 0 °C, after which the subsequent cooling/heating runs maintain this high activity. Without the catalyst pretreatment in O_2, the conversion during the first heating run is lower than in the second one due to the presence of OH-groups and adsorbed water that partially inhibits adsorption of reagents and is released during heating (see Fig. S8). Other inhibiting species, such as carbon-containing impurities, may also be reacted away by O_2 during the first heating cycle. In fact (Fig. 7d), after oxygen pretreatment of the catalyst at 450 °C directly in the reactor, the catalytic activity reaches maximum already at very low temperatures. No activity enhancement is observed for the $1Pt/CeO_2$ catalyst in the second heating run because it oxidizes CO only at temperatures when most of adsorbed water is already released. TPR-CO data (Fig. 4) demonstrate that at the 1 wt% Pt loading mobile ceria lattice oxygen shows up upon interaction with CO at T > 120 °C. For Pt loadings of 8–20 wt%, oxygen from the ceria lattice is more reactive and begins to interact with CO already at room and lower temperatures.

Characterization of the catalysts by XRD, TEM and XPS reveals that metallic platinum is practically absent at all studied compositions; essentially only ionic states Pt^{2+} and Pt^{4+} are observed. Therewith,

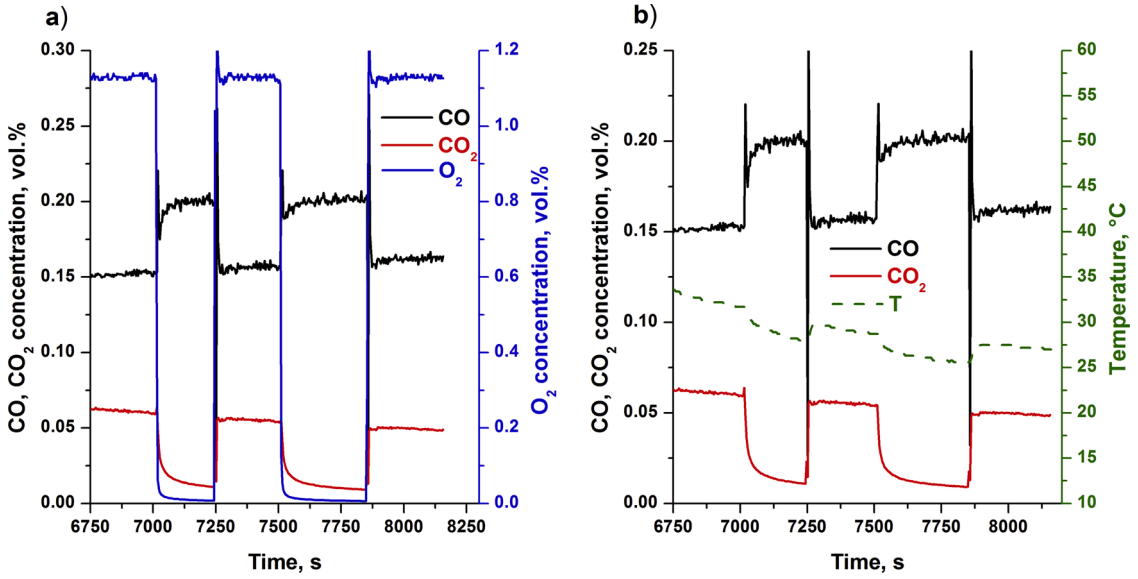

Fig. 11. Data for the catalyst $20Pt/CeO_2$. (a) Concentration of CO, CO_2 and O_2 in the reactor during periods with and without oxygen in the gas supply. (b) CO and CO_2 concentration and temperature during periods with and without O_2 in the gas supply at slow cooling of the reactor to room temperature. The cooling time was significantly longer than the flow relaxation upon on/off O_2 switching.

platinum is maximally dispersed over the surface and some portion of Pt is also incorporated into deeper layers resulting in surface lattice distortions in accordance with XRD and Raman spectroscopy data. A recent study [120] showed that Pt single atoms in the +2 oxidation state are predominantly located at defects and step edges of ceria indicating a local reconstruction of ceria surface with stabilization of the active component as [Pt^{2+}-O_4] species. The latter are incapable to trigger CO oxidation at room temperature and below in line with our experimental data and theoretical results revealing high stability of Pt^{2+} ions on the surface of nanostructured CeO_2 [22,29]. Given that the Pt4f spectra of the catalysts 8Pt/CeO_2 and 20Pt/CeO_2 evidence the presence of both Pt^{2+} and Pt^{4+} species distributed over surface and near-surface regions of ceria, the release of oxygen at T < 120 °C has to be related to these Pt^{4+} and Pt^{2+} ions, which account for the lattice micro-distortions of ceria nanoparticles and generation of mobile oxygen [28]. In this paper the formation of PtO_x clusters with a Pt_3O_4-like structure was suggested at higher Pt loadings. Such PtO_x clusters were proposed to be stabilized in distorted surface/subsurface area of ceria and within the crystalline boundaries. Our DFT results (Sect. 3.6) explain how Pt^{4+} ions help to generate mobile oxygen and why the reduction $Pt^{4+} \rightarrow Pt^{2+}$ becomes disfavored in Pt/CeO_2 nanostructures *vs* the reduction $2Ce^{4+} \rightarrow 2Ce^{3+}$.

The predominant oxidation states of Pt in highly-loaded catalysts are Pt^{2+} and Pt^{4+}; there, the concentration of Ce^{3+} ions Ce^{3+}/Ce is ~10−12 % (Table S2). According to the *ex-situ* XPS data (Fig. 5), the surface concentration of Ce^{3+}, Pt^{2+}, and Pt^{4+} remains virtually constant upon the abundant removal of lattice O atoms during stepwise reduction in CO below 150 °C. Pt^{4+} ions disappear only at higher temperatures concomitantly with concentration increase of metallic platinum and Ce^{3+}. The almost constant Pt^{4+} concentration below 150 °C suggests that migration of O atoms from subsurface regions onto the surface is faster than the removal of surface O by adsorbed CO. This maintains a steady-state oxygen concentration (and corresponding Ce^{3+}/Ce ratio) in surface/subsurface regions under long enough step-by-step XPS experiments. This situation holds until temperature reaches 150 °C, when strong decrease of Pt^{4+} concentration and increase of Ce^{3+} concentration occur due to excessive oxygen removal. After this point, further release of active oxygen is hindered and Pt^{4+} ions are reduced to more stable Pt^{2+} ions. Pt^{4+} peaks vanish from the Pt4f spectra at 250 °C, whereas the peaks of Pt^{2+} remain present even at 450 °C.

Thus, the introduction of platinum in CeO_2 activates its lattice oxygen by making it mobile in the surface/subsurface positions and active for interaction with CO. This decreases the temperature onset of the reaction with CO and increases the amount of CO_2 produced in the low-temperature region (< 100 °C) in comparison with pure CeO_2. The ratio CO_2/Pt ~ 2 (Fig. 4b) shows that ca. two O atoms can be released per each Pt ion (Pt^{2+} or Pt^{4+}). The activation of lattice oxygen by solely Pt^{2+} ions is however indistinguishable from the activation by solely Pt^{4+} ions. This agrees with the suggested formation of PtO_x clusters such as Pt_3O_4/CeO_2 (surface) in highly loaded by Pt ceria samples containing both Pt^{2+} and Pt^{4+} ions [28]. The apparently synergetic action of the latter is crucial for the formation of surface PtO_x-structures required for the low-temperature catalytic oxidation of CO to occur. However, CO oxidation mediated solely by oxygen from near-surface areas of ceria at/below room temperature is slow. Thus, this route is capable of producing only a very minor part of CO_2 formed overall under stationary CO + O_2 conditions at room and lower temperatures.

4.2. CO oxidation at temperatures below 0 °C

For catalysts with low Pt loading, such as 1Pt/CeO_2, the reaction is known to proceed through the Mars–van Krevelen (MvK) mechanism on single-atom [Pt^{2+}-O_4] sites at temperatures > 120 °C [32,39,45,127]. For the 8Pt/CeO_2 and 20Pt/CeO_2 catalysts, the appearance of additional mobile and reactive oxygen due to the action of Pt^{2+} and Pt^{4+} ions increases the efficiency of the MvK mechanism, which can operate already at room temperature. However, high CO conversion observed *below* 0 °C upon Pt loading increase in the catalysts is not due to the MvK mechanism involving oxide lattice oxygen in the CO oxidation. Data in Fig. 9 show that in the temperature range 50–120 °C, the MvK mechanism has a substantial contribution, with a clear increase of CO_2 evolution at these temperatures in the TPR-CO experiments. Nevertheless, this increased mobility of lattice O alone cannot explain the CO oxidation activity below room temperature, because at 0 °C the CO oxidation rate drops to almost zero in absence of gas-phase O_2.

It should be noted that steps corresponding to the adsorption and dissociation of O_2 molecules are also part of the MvK mechanism and are responsible for healing the oxygen vacancies generated upon extraction of lattice O atoms with CO. Such extraction is, however, not possible at low temperatures, as evidenced by the higher light-off temperatures for the oxidation of CO in absence of O_2. In addition, the coincidence of the reduction and total reaction rates when operating through the MvK mechanism further supports that vacancy healing by O_2 does not control the stationary rate of the MvK mechanism. Therefore, the contribution of the MvK mechanism to the overall rate of CO oxidation varies with temperature – above 100 °C the reaction mainly proceeds through the MvK mechanism with the participation of lattice oxygen, between 0 °C and 100 °C both mechanisms contribute to the overall rate of reaction, and at temperatures lower than 0 °C the mechanism with the participation of weakly bound states of CO and O_2 becomes prevalent.

The total CO oxidation rate in TPR-CO + O_2 significantly exceeds that of the MvK mechanism (in TPR-CO) in the temperature range –50 ÷ +50 °C. High CO conversion at room temperature and below therefore has to be due to direct participation of gas-phase O_2, as supported by our experiments with interruption of the O_2 flow. The experiments with CO + O_2 admission at -40 °C (Fig. 10) show a fast response of CO_2 formation for the catalyst fully pre-oxidized at 450 °C. It indicates that after such strong oxidative pretreatment the catalyst can adsorb CO and O_2 only as a weakly bound species. As a consequence, the main oxidation route below room temperature may be related to the co-adsorption and reaction of weakly bound CO and O_2. In general, weak bonding of adsorbed CO is beneficial to prevent inhibition effects [112]. Weakly bound CO can be present, for instance, in surface species $Pt^{2+}(CO)_2$ stabilized by interactions with low-coordinated oxygen atoms exposed on ceria nanoparticles [60]. Weak molecular O_2 adsorption can occur on oxygen vacancies [95], on exposed Ce^{3+} sites [128] or elsewhere. In case the sites for CO and O_2 adsorption are located close to each other the reaction rate can be significantly enhanced due to the formation of CO^*O_2 (or $(CO)_2^*O_2$) reactive complexes [129], the concentration of which should increase at low temperatures [130].

Oxidation reactions at low temperatures without the need to overcome high barriers of O_2 dissociation are quite common [131]. For instance, very low barriers calculated by DFT and high TOF values for the two-stage reaction $CO^* + O_2^* \rightarrow OCOO^* + * \rightarrow CO_2 + O^* + *$ (* denotes an active surface site) [132,133] revealed that it is the fastest route of aerobic CO oxidation on metallic Au/Ag sites occurring even below -50ºC. There, during reaction of very weakly co-adsorbed CO and O_2 the latter might acquire negative charge resulting in more easily breakable longer O—O bonds. However, such peroxide-like species were not observed for the most active 8Pt/CeO_2 and 20Pt/CeO_2 catalysts.

A common feature of reactions on weakly bound states is very low activation energy, as is observed for CO oxidation on our high-percentage Pt/CeO_2 catalysts. Notably, the dip in CO_2 evolution at 50–75 °C in the TPR-CO + O_2 data (Figs. 7b–d and 9) indicates that the low-temperature mechanism loses efficiency upon increasing temperature because of partial desorption of the weakly bound reactants.

The weak adsorption of CO and O_2 with their subsequent reaction takes place only on ceria containing increased amount of platinum (8 % and more). Active sites on these catalysts are different from those in catalysts with low Pt loadings. In the latter, the single-atom Pt^{2+} sites are expected to be separated by rather long distances, while in highly Pt-loaded catalysts the density of surface centers for CO and O_2 adsorption significantly increases. Increased concentration of Pt on the ceria

surface, which takes place for the 8Pt/CeO_2 and 20Pt/CeO_2 catalysts, has been reported by TEM to facilitate the formation of Pt_nO_m surface clusters on CeO_2 [28], e.g. *via* theoretically proposed PtO precursors [134]. Such association can be considered as a phase transition from the atomically dispersed Pt in [Pt^{2+}-O_4] moieties to small Pt_nO_m clusters interacting with the surface of ceria [56]. We therefore propose that clustering of oxidized Pt atoms forming PtO_x moieties is required for the low-temperature oxidation mechanism. A key feature of such Pt_nO_m clusters compared with the single-atom sites is the presence of additional Pt-O-Pt bonds along with preserved Pt-O-Ce bonds on the PtO_x boundary [56].

Gatla et al. [103,135], Ganzler et al. [47,48,136], Pilger et al. [46, 137] and Pereira-Hernández et al. [34] communicated transformations of ionic Pt species to metallic Pt_n clusters in Pt/CeO_2 catalysts for CO oxidation under H_2 or CO treatment. Such reduction of the Pt/CeO_2 catalysts resulted in noticeable increase of the CO oxidation activity. Similar results have been published recently by Grunwaldt et al. [49], where metallic Pt clusters formed from single atom sites under reaction conditions become more active than the resting state with atomically dispersed Pt. However, this activity increase was reported only well above room temperature. In turn, our experiments reveal activity at 0 °C and lower temperatures for the highly loaded Pt samples treated in O_2 or in the reaction mixture up to 450 °C. The formation of PtO_x upon this treatment is consistent with the high CO oxidation activity reported by Ke et al. [45] for PtO_x clusters supported on ceria nanowires, where partial reduction of the PtO_x clusters provided very active undercoordinated sites. Moreover, we obtain very similar TPR-CO and TPR-H_2 data to those obtained by Ke et al. [45] on the PtO_x supported on ceria nanowires, which further indicates that PtO_x clusters are formed on our catalysts with high Pt-loading.

The present study demonstrates that interplay of Pt^{2+} and Pt^{4+} species with nanostructured ceria enables preparation of CO oxidation catalysts highly efficient well below room temperature. Our results suggest that such extraordinary catalytic features at very low temperature are related to the presence of PtO_x/CeO_2 structures.

5. Conclusions

In this work, we systematically studied Pt/CeO_2 catalysts with varying Pt loading (1, 8, and 20 wt%) prepared by precipitation and calcination. The low Pt-loaded (1 wt%) catalyst is active towards the CO oxidation reaction only at T > 120 °C, while the catalysts with higher Pt loadings (8–20 wt%) showed activity for CO oxidation well below 0 °C. The different activity of the catalysts with higher Pt loading can be traced back to differences in the location and oxidation states of the Pt content. XRD, HRTEM, and XPS data indicate that whereas 1 wt% Pt loading leads only to single-atom Pt^{2+} species dispersed on the surface of ceria nanoparticle, higher Pt loadings result in a high concentration of Pt^{2+} (both in surface sites and within distorted boundaries of ceria crystallites) and Pt^{4+} ions (mostly in the ceria lattice), with a fraction of the ionic Pt content likely aggregated into PtO_x clusters.

Raman spectroscopy, kinetic experiments, and DFT calculations indicate that the Pt^{4+} and Pt^{2+} cations distort the ceria lattice and facilitate the release and migration of O from ceria. This lowers the light-off temperature of the MvK mechanism operating mainly on single-atom Pt^{2+} sites, but is incapable of providing alone an efficient stationary catalysis at very low temperatures (<0 °C). The reaction on the highly loaded catalyst at very low T is instead considered to involve weakly adsorbed O_2 and CO molecules reacting on ceria-supported PtO_x clusters. Further improvements aimed at decreasing the catalysts cost for practical applications could be achieved e.g. by deposition of Pt-ceria active component on high surface area supports or by generating the same active sites at lower Pt loadings, which we have shown is possible by diluting catalysts with higher Pt loading. The deeper understanding gained in this work regarding the interplay of different states of platinum on ceria provides design principles for engineering catalytically active sites able to mediate low-temperature oxidation reactions.

CRediT authorship contribution statement

Andrei I. Boronin: Conceptualization, Writing - original draft. **Elena M. Slavinskaya:** Investigation, Writing - original draft. **Alberto Figueroba:** Investigation. **Andrey I. Stadnichenko:** Investigation. **Tatyana Yu. Kardash:** Investigation. **Olga A. Stonkus:** Investigation. **Elizaveta A. Fedorova:** Investigation. **Valerii V. Muravev:** Investigation. **Valery A. Svetlichnyi:** Investigation. **Albert Bruix:** Investigation, Writing - review & editing. **Konstantin M. Neyman:** Methodology, Writing - review & editing.

Declaration of Competing Interest

The authors report no declarations of interest.

Acknowledgements

This work was supported by the Ministry of Science and Higher Education of the Russian Federation within the governmental order for Boreskov Institute of Catalysis (project AAAA-A21-121011390053-4). AB and KMN gratefully acknowledge support by the Spanish government grants PGC2018-093863-B-C22, MDM-2017-0767, PRX17/00348 and the grants 2018BP00190 and 2017SGR13 of the Generalitat de Catalunya. They also thank the Red Española de Supercomputación for providing computer resources as well as the European Cooperation in Science and Technology program via the COST Action CA18234 for stimulating the present study.

Appendix A. Supplementary data

Supplementary material related to this article can be found, in the online version, at doi:https://doi.org/10.1016/j.apcatb.2021.119931.

References

[1] H.S. Gandhi, G.W. Graham, R.W. McCabe, Automotive exhaust catalysis, J. Catal. 216 (2003) 433–442.
[2] G. Germani, P. Alphonse, M. Courty, Y. Schuurman, C. Mirodatos, Platinum/ceria/alumina catalysts on microstructures for carbon monoxide conversion, Catal. Today 110 (2005) 114–120.
[3] W. Yu, M.D. Porosoff, J.G. Chen, Review of Pt-based bimetallic catalysis: from model surfaces to supported catalysts, Chem. Rev. 112 (2012) 5780–5817.
[4] D. Pierre, W. Deng, M. Flytzani-Stephanopoulos, The importance of strongly bound Pt-CeO_x species for the water-gas shift reaction: catalyst activity and stability evaluation, Top. Catal. 46 (2007) 363–373.
[5] K. Liu, A. Wang, T. Zhang, Recent advances in preferential oxidation of CO reaction over platinum group metal catalysts, ACS Catal. 2 (2012) 1165–1178.
[6] O. Pozdnyakova-Tellinger, D. Teschner, J. Kröhnert, F.C. Jentoft, A. Knop-Gericke, R. Schlögl, A. Wootsch, Surface water-assisted preferential CO oxidation on Pt/CeO_2 catalyst, J. Phys. Chem. C 111 (2007) 5426–5431.
[7] F. Morfin, T.-S. Nguyen, J.-L. Rousset, L. Piccolo, Synergy between hydrogen and ceria in Pt-catalyzed CO oxidation: an investigation on Pt–CeO_2 catalysts synthesized by solution combustion, Appl. Catal. B: Environ. 197 (2016) 2–13.
[8] J.B. Park, J. Graciani, J. Evans, D. Stacchiola, S.D. Senanayake, L. Barrio, P. Liu, J.F. Sanz, J. Hrbek, J.A. Rodriguez, Gold, copper, and platinum nanoparticles dispersed on CeO_x/TiO_2(110) surfaces: high water-gas shift activity and the nature of the mixed-metal oxide at the nanometer level, J. Am. Chem. Soc. 132 (2010) 356–363.
[9] R. Tiwari, B. Sarkar, R. Tiwari, C. Pendem, T. Sasaki, S. Saran, R. Bal, Pt nanoparticles with tuneable size supported on nanocrystalline ceria for the low temperature water-gas-shift (WGS) reaction, J. Mol. Catal. A Chem. 395 (2014) 117–123.
[10] A. Goguet, S.O. Shekhtman, R. Burch, C. Hardacre, F.C. Meunier, G.S. Yablonsky, Pulse-response TAP studies of the reverse water–gas shift reaction over a Pt/CeO_2 catalyst, J. Catal. 237 (2006) 102–110.
[11] C.M. Kalamaras, S. Americanou, A.M. Efstathiou, "Redox" vs "associative formate with –OH group regeneration" WGS reaction mechanism on Pt/CeO_2: effect of platinum particle size, J. Catal. 279 (2011) 287–300.
[12] S.C. Ammal, A. Heyden, Understanding the nature and activity of supported platinum catalysts for the water–gas shift reaction: from metallic nanoclusters to alkali-stabilized single-atom cations, ACS Catal. 9 (2019) 7721–7740.

[13] G. Jacobs, P.M. Patterson, U.M. Graham, A.C. Crawford, B.H. Davis, Low temperature water gas shift: the link between the catalysis of WGS and formic acid decomposition over Pt/ceria, Int. J. Hydrogen Energy 30 (2005) 1265–1276.

[14] Y. Zheng, Y. Zheng, Y. Xiao, G. Cai, K. Wei, The effect of nickel on propane oxidation and sulfur resistance of $Pt/Ce_{0.4}Zr_{0.6}O_2$ catalyst, Catal. Commun. 39 (2013) 1–4.

[15] P.L. Silveston, W.S. Epling, in: P.L. Silveston, R.R. Hudgins (Eds.), Periodic Operation of Chemical Reactors, Butterworth-Heinemann, Oxford, 2013, pp. 141–170.

[16] S.J. Tauster, S.C. Fung, R.T.K. Baker, J.A. Horsley, Strong interactions in supported-metal catalysts, Science 211 (1981) 1121–1125.

[17] A. Bruix, J.A. Rodriguez, P.J. Ramírez, S.D. Senanayake, J. Evans, J.B. Park, D. Stacchiola, P. Liu, J. Hrbek, F. Illas, A new type of strong metal–support interaction and the production of H_2 through the transformation of water on $Pt/CeO_2(111)$ and $Pt/CeO_x/TiO_2(110)$ catalysts, J. Am. Chem. Soc. 134 (2012) 8968–8974.

[18] J. Kaspar, P. Fornasiero, M. Graziani, Use of CeO_2-based oxides in the three-way catalysis, Catal. Today 50 (1999) 285–298.

[19] M. Shelef, R.W. McCabe, Twenty-five years after introduction of automotive catalysts: what next? Catal. Today 62 (2000) 35–50.

[20] T. Montini, M. Melchionna, M. Monai, P. Fornasiero, Fundamentals and catalytic applications of CeO_2-based materials, Chem. Rev. 116 (2016) 5987–6041.

[21] M. Ozawa, M. Misaki, M. Iwakawa, M. Hattori, K. Kobayashi, K. Higuchi, S. Arai, Low content Pt-doped CeO_2 and core-shell type CeO_2/ZrO_2 model catalysts; microstructure, TPR and three way catalytic activities, Catal. Today 332 (2019) 251–258.

[22] A. Bruix, Y. Lykhach, I. Matolínová, A. Neitzel, T. Skála, N. Tsud, M. Vorokhta, V. Stetsovych, K. Ševčíková, J. Mysliveček, R. Fiala, M. Václavů, K.C. Prince, S. Bruyère, V. Potin, F. Illas, V. Matolín, J. Libuda, K.M. Neyman, Maximum noble-metal efficiency in catalytic materials: atomically dispersed surface platinum, Angew. Chem., Int. Ed. 53 (2014) 10525–10530.

[23] P. Bera, K.C. Patil, V. Jayaram, G.N. Subbanna, M.S. Hegde, Ionic dispersion of Pt and Pd on CeO_2 by combustion method: effect of metal–ceria interaction on catalytic activities for NO reduction and CO and hydrocarbon oxidation, J. Catal. 196 (2000) 293.

[24] Q. Fu, H. Saltsburg, M. Flytzani-Stephanopoulos, Active nonmetallic Au and Pt species on ceria-based water-gas shift catalysts, Science 301 (2003) 935–938.

[25] M.S. Hegde, P. Bera, Noble metal ion substituted CeO_2 catalysts: electronic interaction between noble metal ions and CeO_2 lattice, Catal. Today 253 (2015) 40–50.

[26] M.S. Hegde, G. Madras, K.C. Patil, Noble metal ionic catalysts, Acc. Chem. Res. 42 (2009) 704–712.

[27] E.M. Slavinskaya, R.V. Gulyaev, A.V. Zadesenets, O.A. Stonkus, V.I. Zaikovskii, Y. V. Shubin, S.V. Korenev, A.I. Boronin, Low-temperature CO oxidation by Pd/CeO_2 catalysts synthesized using the coprecipitation method, Appl. Catal. B: Environ. 166–167 (2015) 91–103.

[28] E.A. Derevyannikova, T.Y. Kardash, A.I. Stadnichenko, O.A. Stonkus, E. M. Slavinskaya, V.A. Svetlichnyi, A.I. Boronin, Structural insight into strong $Pt–CeO_2$ interaction: from single Pt atoms to PtO_x clusters, J. Phys. Chem. C 123 (2019) 1320–1334.

[29] A. Figueroba, G. Kovacs, A. Bruix, K.M. Neyman, Towards stable single-atom catalysts: strong binding of atomically dispersed transition metals on the surface of nanostructured ceria, Catal. Sci. Technol. 6 (2016) 6806–6813.

[30] A. Neitzel, A. Figueroba, Y. Lykhach, T. Skála, M. Vorokhta, N. Tsud, S. Mehl, K. Ševčíková, K.C. Prince, K.M. Neyman, V. Matolín, J. Libuda, Atomically dispersed Pd, Ni, and Pt species in ceria-based catalysts: principal differences in stability and reactivity, J. Phys. Chem. C 120 (2016) 9852–9862.

[31] J. Jones, H. Xiong, A.T. DeLaRiva, E.J. Peterson, H. Pham, S.R. Challa, G. Qi, S. Oh, M.H. Wiebenga, X.I. Pereira Hernández, Y. Wang, A.K. Datye, Thermally stable single-atom platinum-on-ceria catalysts via atom trapping, Science 353 (2016) 150–154.

[32] L. Nie, D. Mei, H. Xiong, B. Peng, Z. Ren, X.I.P. Hernandez, A. DeLaRiva, M. Wang, M.H. Engelhard, L. Kovarik, A.K. Datye, Y. Wang, Activation of surface lattice oxygen in single-atom Pt/CeO_2 for low-temperature CO oxidation, Science 358 (2017) 1419–1423.

[33] X.I. Pereira Hernández, A.T. DeLaRiva, H. Xiong, D. Kunwar, E.J. Peterson, A. K. Datye, Y. Wang, B. Sudduth, Reversible transformation from Pt single atoms to sub-nanometer particles for low temperature CO oxidation, in: AIChE Annual Meeting, Minneapolis; United States, 2017, pp. 75–78.

[34] X.I. Pereira-Hernández, A. DeLaRiva, V. Muravev, D. Kunwar, H. Xiong, B. Sudduth, M. Engelhard, L. Kovarik, E.J.M. Hensen, Y. Wang, A.K. Datye, Tuning $Pt-CeO_2$ interactions by high-temperature vapor-phase synthesis for improved reducibility of lattice oxygen, Nat. Commun. 10 (2019) 1358.

[35] S. Shimada, T. Takei, T. Akita, S. Takeda, M. Haruta, in: E.M. Gaigneaux, M. Devillers, S. Hermans, P.A. Jacobs, J.A. Martens, P. Ruiz (Eds.), Studies in Surface Science and Catalysis, Elsevier, 2010, pp. 843–847.

[36] M. Cargnello, V.V.T. Doan-Nguyen, T.R. Gordon, R.E. Diaz, E.A. Stach, R.J. Gorte, P. Fornasiero, C.B. Murray, Control of metal nanocrystal size reveals metal-support interface role for ceria catalysts, Science 341 (2013) 771–773.

[37] S.K. Meher, M. Cargnello, H. Troiani, T. Montini, G.R. Rao, P. Fornasiero, Alcohol induced ultra-fine dispersion of Pt on tuned morphologies of CeO_2 for CO oxidation, Appl. Catal. B: Environ. 130–131 (2013) 121–131.

[38] K. An, S. Alayoglu, N. Musselwhite, S. Plamthottam, G. Melaet, A.E. Lindeman, G. A. Somorjai, Enhanced CO oxidation rates at the interface of mesoporous oxides and Pt nanoparticles, J. Am. Chem. Soc. 135 (2013) 16689–16696.

[39] H.-H. Liu, Y. Wang, A.-P. Jia, S.-Y. Wang, M.-F. Luo, J.-Q. Lu, Oxygen vacancy promoted CO oxidation over Pt/CeO_2 catalysts: a reaction at $Pt–CeO_2$ interface, Appl. Surf. Sci. 314 (2014) 725–734.

[40] P. Bera, A. Gayen, M.S. Hegde, N.P. Lalla, L. Spadaro, F. Frusteri, F. Arena, Promoting effect of CeO_2 in combustion synthesized Pt/CeO_2 catalyst for CO oxidation, J. Phys. Chem. B 107 (2003) 6122–6130.

[41] A.I. Boronin, E.M. Slavinskaya, I.G. Danilova, R.V. Gulyaev, Y.I. Amosov, P. A. Kuznetsov, I.A. Polukhina, S.V. Koscheev, V.I. Zaikovskii, A.S. Noskov, Investigation of palladium interaction with cerium oxide and its state in catalysts for low-temperature CO oxidation, Catal. Today 144 (2009) 201–211.

[42] R.V. Gulyaev, A.I. Stadnichenko, E.M. Slavinskaya, A.S. Ivanova, S.V. Koscheev, A.I. Boronin, In situ preparation and investigation of Pd/CeO_2 catalysts for the low-temperature oxidation of CO, Appl. Catal. A Gen. 439–440 (2012) 41–50.

[43] R.V. Gulyaev, E.M. Slavinskaya, S.A. Novopashin, D.V. Smovzh, A.V. Zaikovskii, D.Y. Osadchii, O.A. Bulavchenko, S.V. Korenev, A.I. Boronin, Highly active $PdCeO_x$ composite catalysts for low-temperature CO oxidation, prepared by plasma-arc synthesis, Appl. Catal. B: Environ. 147 (2014) 132–143.

[44] E.M. Slavinskaya, T.Y. Kardash, O.A. Stonkus, R.V. Gulyaev, I.N. Lapin, V. A. Svetlichnyi, A.I. Boronin, Metal-support interaction in Pd/CeO_2 model catalysts for CO oxidation: from pulsed laser-ablated nanoparticles to highly active state of the catalyst, Catal. Sci. Technol. 6 (2016) 6650–6666.

[45] J. Ke, W. Zhu, Y. Jiang, R. Si, Y.-J. Wang, S.-C. Li, C. Jin, H. Liu, W.-G. Song, C.-H. Yan, Y.-W. Zhang, Strong local coordination structure effects on subnanometer PtO_x clusters over CeO_2 nanowires probed by low-temperature CO oxidation, ACS Catal. 5 (2015) 5164–5173.

[46] F. Pilger, A. Testino, A. Carino, C. Proff, A. Kambolis, A. Cervellino, C. Ludwig, Size control of Pt clusters on CeO_2 nanoparticles via an incorporation–segregation mechanism and study of segregation kinetics, ACS Catal. 6 (2016) 3688–3699.

[47] A.M. Gänzler, M. Casapu, P. Vernoux, S. Loridant, F.J. Cadete Santos Aires, T. Epicier, B. Betz, R. Hoyer, J.-D. Grunwaldt, Tuning the structure of platinum particles on ceria in-situ for enhancing the catalytic performance of exhaust gas catalysts, Angew. Chem. Int. Ed. 56 (2017) 13078–13082.

[48] A.M. Gänzler, M. Casapu, F. Maurer, H. Störmer, D. Gerthsen, G. Ferré, P. Vernoux, B. Bornmann, R. Frahm, V. Murzin, M. Nachtegaal, M. Votsmeier, J.-D. Grunwaldt, Tuning the Pt/CeO_2 interface by in-situ variation of the Pt particle size, ACS Catal. 8 (2018) 4800–4811.

[49] F. Maurer, J. Jelic, J. Wang, A. Gänzler, P. Dolcet, C. Wöll, Y. Wang, F. Studt, M. Casapu, J.-D. Grunwaldt, Tracking the formation, fate and consequence for catalytic activity of Pt single sites on CeO_2, Nat. Catal. 3 (2020) 824–833.

[50] K. Ding, A. Gulec, A.M. Johnson, N.M. Schweitzer, G.D. Stucky, L.D. Marks, P. C. Stair, Identification of active sites in CO oxidation and water-gas shift over supported Pt catalysts, Science 350 (2015) 189–192.

[51] B. Han, R. Lang, B. Qiao, A. Wang, T. Zhang, Highlights of the major progress in single-atom catalysis in 2015 and 2016, Chin. J. Catal. 38 (2017) 1498–1507.

[52] S. Song, Y. Wu, S. Ge, L. Wang, Y. Wang, Y. Guo, W. Zhan, Y. Guo, A facile way to improve Pt atom efficiency for CO oxidation at low temperature: modification by transition metal oxides, ACS Catal. 9 (2019) 6177–6187.

[53] J. Chen, Y. Wanyan, J. Zeng, H. Fang, Z. Li, Y. Dong, R. Qin, C. Wu, D. Liu, M. Wang, Q. Kuang, Z. Xie, L. Zheng, Surface engineering protocol to obtain an atomically dispersed Pt/CeO_2 catalyst with high activity and stability for CO oxidation, ACS Sustain. Chem. Eng. 6 (2018) 14054–14062.

[54] L. DeRita, S. Dai, K. Lopez-Zepeda, N. Pham, G.W. Graham, X. Pan, P. Christopher, Catalyst architecture for stable single atom dispersion enables site-specific spectroscopic and reactivity measurements of CO adsorbed to Pt atoms, oxidized Pt clusters, and metallic Pt clusters on TiO_2, J. Am. Chem. Soc. 139 (2017) 14150–14165.

[55] E.D. Goodman, A.C. Johnston-Peck, E.M. Dietze, C.J. Wrasman, A.S. Hoffman, F. Abild-Pedersen, S.R. Bare, P.N. Plessow, M. Cargnello, Catalyst deactivation via decomposition into single atoms and the role of metal loading, Nat. Catal. 2 (2019) 748–755.

[56] H. Wang, J.-X. Liu, L.F. Allard, S. Lee, J. Liu, H. Li, J. Wang, J. Wang, S.H. Oh, W. Li, M. Flytzani-Stephanopoulos, M. Shen, B.R. Goldsmith, M. Yang, Surpassing the single-atom catalytic activity limit through paired Pt-O-Pt ensemble built from isolated Pt_1 atoms, Nat. Commun. 10 (2019) 3808.

[57] Z.W. Chen, L.X. Chen, C.C. Yang, Q. Jiang, Atomic (single, double, and triple atoms) catalysis: frontiers, opportunities, and challenges, J. Mater. Chem. A 7 (2019) 3492–3515.

[58] J. Li, Y. Tang, Y. Ma, Z. Zhang, F. Tao, Y. Qu, In situ formation of isolated bimetallic PtCe sites of single-dispersed Pt on CeO_2 for low-temperature CO oxidation, ACS Appl. Mater. Interfaces 10 (2018) 38134–38140.

[59] Y.-Q. Su, Y. Wang, J.-X. Liu, I.A.W. Filot, K. Alexopoulos, L. Zhang, V. Muravev, B. Zijlstra, D.G. Vlachos, E.J.M. Hensen, Theoretical approach to predict the stability of supported single-atom catalysts, ACS Catal. 9 (2019) 3289–3297.

[60] I.Z. Koleva, H.A. Aleksandrov, G.N. Vayssilov, Decomposition behavior of platinum clusters supported on ceria and γ-alumina in the presence of carbon monoxide, Catal. Sci. Technol. 7 (2017) 734–742.

[61] N. Daelman, M. Capdevila-Cortada, N. López, Dynamic charge and oxidation state of Pt/CeO_2 single-atom catalysts, Nat. Mater. 18 (2019) 1215–1221.

[62] X. Hong, Y. Sun, Effect of preparation methods on the performance of Pt/CeO_2 catalysts for the catalytic oxidation of carbon monoxide, Catal. Lett. 146 (2016) 2001–2008.

[63] L. Liu, A. Corma, Metal catalysts for heterogeneous catalysis: from single atoms to nanoclusters and nanoparticles, Chem. Rev. 118 (2018) 4981–5079.

[64] A. Beniya, S. Higashi, Towards dense single-atom catalysts for future automotive applications, Nat. Catal. 2 (2019) 590–602.

[65] D. Briggs, Practical Surface Analysis by Auger and X-ray Photoelectron Spectroscopy, Wiley, Chichester, 1983.
[66] J. El Fallah, L. Hilaire, M. Roméo, F. Le Normand, Effect of surface treatments, photon and electron impacts on the ceria 3d core level, J. Electron Spectrosc. Relat. Phenom. 73 (1995) 89–103.
[67] D. Briggs, Handbook of X-ray Photoelectron Spectroscopy, C. D. Wanger, W. M. Riggs, L. E. Davis, J. F. Moulder and G. E. Muilenberg Perkin-Elmer Corp., Physical Electronics Division, Eden Prairie, Minnesota, USA, 1979, 190 pp.
[68] D.A. Svintsitskiy, L.S. Kibis, A.I. Stadnichenko, S.V. Koscheev, V.I. Zaikovskii, A. I. Boronin, Highly oxidized platinum nanoparticles prepared through radio-frequency sputtering: thermal stability and reaction probability towards CO, ChemPhysChem 16 (2015) 3318–3324.
[69] A.I. Stadnichenko, V.V. Murav'ev, V.A. Svetlichnyi, A.I. Boronin, Platinum state in highly active Pt/CeO_2 catalysts from the X-ray photoelectron spectroscopy data, J. Struct. Chem. 58 (2017) 1152–1159.
[70] TOPAS, Version 4.2., Bruker AXS Inc., Madison, Wisconsin, USA, 2009.
[71] D.A. Svintsitskiy, I.Y. Pakharukov, E.M. Slavinskaya, T.Y. Kardash, V.N. Parmon, A.I. Boronin, Influence of the copper(II) oxide dispersion on its catalytic properties in carbon monoxide oxidation: a comparative study by using two types of catalytic reactors, ChemCatChem 8 (2016) 3546–3555.
[72] E.M. Slavinskaya, O.A. Stonkus, R.V. Gulyaev, A.S. Ivanova, V.I. Zaikovskii, P. A. Kuznetsov, A.I. Boronin, Structural and chemical states of palladium in Pd/Al_2O_3 catalysts under self-sustained oscillations in reaction of CO oxidation, Appl. Catal. A Gen. 401 (2011) 83–97.
[73] G. Kresse, J. Hafner, Ab initio molecular dynamics for liquid metals, Phys. Rev. B 47 (1993) 558–561.
[74] G. Kresse, J. Furthmuller, Efficient iterative schemes for ab initio total-energy calculations using a plane-wave basis set, Phys. Rev. B 54 (1996) 11169.
[75] J.P. Perdew, J.A. Chevary, S.H. Vosko, K.A. Jackson, M.R. Pederson, D.J. Singh, C. Fiolhais, Atoms, molecules, solids, and surfaces: applications of the generalized gradient approximation for exchange and correlation, Phys. Rev. B 46 (1992) 6671–6687.
[76] J.P. Perdew, J.A. Chevary, S.H. Vosko, K.A. Jackson, M.R. Pederson, D.J. Singh, C. Fiolhais, Erratum: Atoms, molecules, solids, and surfaces: applications of the generalized gradient approximation for exchange and correlation, Phys. Rev. B 48 (1993) 4978.
[77] V.I. Anisimov, F. Aryasetiawan, A.I. Lichtenstein, First-principles calculations of the electronic structure and spectra of strongly correlated systems: the LDA + U method, J. Phys. Condens. Matter 9 (1997) 767.
[78] A. Migani, G.N. Vayssilov, S.T. Bromley, F. Illas, K.M. Neyman, Dramatic reduction of the oxygen vacancy formation energy in ceria particles: a possible key to their remarkable reactivity at the nanoscale, J. Mater. Chem. 20 (2010) 10535–10546.
[79] G.N. Vayssilov, Y. Lykhach, A. Migani, T. Staudt, G.P. Petrova, N. Tsud, T. Skála, A. Bruix, F. Illas, K.C. Prince, V. Matolín, K.M. Neyman, J. Libuda, Support nanostructure boosts oxygen transfer to catalytically active platinum nanoparticles, Nat. Mater. 10 (2011) 310–315.
[80] C. Loschen, J. Carrasco, K.M. Neyman, F. Illas, First-principles LDA+U and GGA+U study of cerium oxides: dependence on the effective U parameter, Phys. Rev. B 75 (2007), 035115.
[81] P.E. Blöchl, Projector augmented-wave method, Phys. Rev. B 50 (1994) 17953.
[82] S.M. Kozlov, H.A. Aleksandrov, J. Goniakowski, K.M. Neyman, Effect of MgO (100) support on structure and properties of Pd and Pt nanoparticles with 49-155 atoms, J. Chem. Phys. 139 (2013), 084701.
[83] F. Viñes, F. Illas, K.M. Neyman, On the mechanism of formation of metal nanowires by self-assembly, Angew. Chem., Int. Ed. 46 (2007) 7094–7097.
[84] A. Bruix, K.M. Neyman, Modeling ceria-based nanomaterials for catalysis and related applications, Catal. Lett. 146 (2016) 2053–2080.
[85] Y. Lykhach, A. Bruix, S. Fabris, V. Potin, I. Matolinova, V. Matolin, J. Libuda, K. M. Neyman, Oxide-based nanomaterials for fuel cell catalysis: the interplay between supported single Pt atoms and particles, Catal. Sci. Technol. 7 (2017) 4315–4345.
[86] A. Bruix, K.M. Neyman, How to design models for ceria nanoparticles: challenges and strategies for describing nanostructured reducible oxides, in: S.T. Bromley, S. M. Woodley (Eds.), Frontiers of Nanoscience, Elsevier, 2018, pp. 55–99.
[87] Powder Diffraction File.PDF-2//Release 2009, // International Centre for Diffraction Data, USA, 2009.
[88] S. Tsunekawa, S. Ito, Y. Kawazoe, Surface structures of cerium oxide nanocrystalline particles from the size dependence of the lattice parameters, Appl. Phys. Lett. 85 (2004) 3845–3847.
[89] A.E. Baranchikov, O.S. Polezhaeva, V.K. Ivanov, Y.D. Tretyakov, Lattice expansion and oxygen non-stoichiometry of nanocrystalline ceria, CrystEngComm 12 (2010) 3531–3533.
[90] S. Colussi, M. Boaro, L. de Rogatis, A. Pappacena, C. de Leitenburg, J. Llorca, A. Trovarelli, Room temperature oxidation of formaldehyde on Pt-based catalysts: a comparison between ceria and other supports (TiO_2, Al_2O_3 and ZrO_2), Catal. Today 253 (2015) 163–171.
[91] R. Fiala, M. Vaclavu, A. Rednyk, I. Khalakhan, M. Vorokhta, J. Lavkova, V. Potin, I. Matolinova, V. Matolin, Pt–CeO_x thin film catalysts for PEMFC, Catal. Today 240 (2015) 236–241.
[92] E. Ozkaraoglu, I. Tunc, S. Suzer, X-ray induced reduction of Au and Pt ions on silicon substrates, Surf. Coat. Technol. 201 (2007) 8202–8204.
[93] A. Trovarelli, Catalytic properties of ceria and CeO_2-containing materials, Catal. Rev. - Sci. Eng. 38 (1996) 439–520.
[94] E. Paparazzo, G.M. Ingo, N. Zacchetti, X-ray induced reduction effects at CeO_2 surfaces: an x-ray photoelectron spectroscopy study, J. Vacuum Sci. Technol. A 9 (1991) 1416–1420.
[95] C. Schilling, M.V. Ganduglia-Pirovano, C. Hess, Experimental and theoretical study on the nature of adsorbed oxygen species on shaped ceria nanoparticles, J. Phys. Chem. Lett. 9 (2018) 6593–6598.
[96] T. Taniguchi, T. Watanabe, N. Sugiyama, A.K. Subramani, H. Wagata, N. Matsushita, M. Yoshimura, Identifying defects in ceria-based nanocrystals by UV resonance Raman spectroscopy, J. Phys. Chem. C 113 (2009) 19789–19793.
[97] L. Li, F. Chen, J.-Q. Lu, M.-F. Luo, Study of defect sites in $Ce_{1-x}M_xO_{2-\delta}$ ($x = 0.2$) solid solutions using Raman spectroscopy, J. Phys. Chem. A 115 (2011) 7972–7977.
[98] W. Lin, A.A. Herzing, C.J. Kiely, I.E. Wachs, Probing metal−support interactions under oxidizing and reducing conditions: in situ Raman and infrared spectroscopic and scanning transmission electron microscopic−X-ray energy-dispersive spectroscopic investigation of supported platinum catalysts, J. Phys. Chem. C 112 (2008) 5942–5951.
[99] M. Ray, J.O. Kafader, J.E. Topolski, C.C. Jarrold, Mixed cerium-platinum oxides: electronic structure of $[CeO]Pt_n$ ($n = 1, 2$) and $[CeO_2]Pt$ complex anions and neutrals, J. Chem. Phys. 145 (2016), 044317.
[100] L.L. Murrell, S.J. Tauster, D.R. Anderson, in: A. Crucq (Ed.), Studies in Surface Science and Catalysis, Elsevier, 1991, pp. 275–289.
[101] M.S. Brogan, T.J. Dines, J.A. Cairns, Raman spectroscopic study of the Pt-CeO_2 interaction in the Pt/Al_2O_3-CeO_2 catalyst, J. Chem. Soc., Faraday Trans. 90 (1994) 1461–1466.
[102] P. Fornasiero, E. Fonda, R. Di Monte, G. Vlaic, J. Kašpar, M. Graziani, Relationships between structural/textural properties and redox behavior in $Ce_{0.6}Zr_{0.4}O_2$ mixed oxides, J. Catal. 187 (1999) 177–185.
[103] S. Gatla, D. Aubert, G. Agostini, O. Mathon, S. Pascarelli, T. Lunkenbein, M. G. Willinger, H. Kaper, Room-temperature CO oxidation catalyst: low-temperature metal–support interaction between platinum nanoparticles and nanosized ceria, ACS Catal. 6 (2016) 6151–6155.
[104] A. Vita, C. Italiano, C. Fabiano, L. Pino, M. Laganà, V. Recupero, Hydrogen-rich gas production by steam reforming of n-dodecane: part I: catalytic activity of Pt/CeO_2 catalysts in optimized bed configuration, Appl. Catal. B: Environ. 199 (2016) 350–360.
[105] Y. Lykhach, S.M. Kozlov, T. Skála, A. Tovt, V. Stetsovych, N. Tsud, F. Dvořák, V. Johánek, A. Neitzel, J. Mysliveček, S. Fabris, V. Matolín, K.M. Neyman, J. Libuda, Counting electrons on supported nanoparticles, Nat. Mater. 15 (2016) 284–288.
[106] A. Bruix, A. Migani, G.N. Vayssilov, K.M. Neyman, J. Libuda, F. Illas, Effects of deposited Pt particles on the reducibility of CeO_2(111), Phys. Chem. Chem. Phys. 13 (2011) 11384–11392.
[107] S.M. Kozlov, K.M. Neyman, Effects of electron transfer in model catalysts composed of Pt nanoparticles on CeO_2(111) surface, J. Catal. 344 (2016) 507–514.
[108] G. Ferré, M. Aouine, F. Bosselet, L. Burel, F.J. Cadete Santos Aires, C. Geantet, S. Ntais, F. Maurer, M. Casapu, J.-D. Grunwaldt, T. Epicier, S. Loridant, P. Vernoux, Exploiting the dynamic properties of Pt on ceria for low-temperature CO oxidation, Catal. Sci. Technol. 10 (2020) 3904–3917.
[109] E.W. McFarland, H. Metiu, Catalysis by doped oxides, Chem. Rev. 113 (2013) 4391–4427.
[110] A. Figueroba, A. Bruix, G. Kovács, K.M. Neyman, Metal-doped ceria nanoparticles: stability and redox processes, Phys. Chem. Chem. Phys. 19 (2017) 21729–21738.
[111] J. Koettgen, S. Grieshammer, P. Hein, B.O.H. Grope, M. Nakayama, M. Martin, Understanding the ionic conductivity maximum in doped ceria: trapping and blocking, Phys. Chem. Chem. Phys. 20 (2018) 14291–14321.
[112] S. Royer, D. Duprez, Catalytic oxidation of carbon monoxide over transition metal oxides, ChemCatChem 3 (2011) 24–65.
[113] D.O. Scanlon, B.J. Morgan, G.W. Watson, The origin of the enhanced oxygen storage capacity of $Ce_{1-x}(Pd/Pt)_xO_2$, Phys. Chem. Chem. Phys. 13 (2011) 4279–4284.
[114] I. Celardo, J.Z. Pedersen, E. Traversa, L. Ghibelli, Pharmacological potential of cerium oxide nanoparticles, Nanoscale 3 (2011) 1411–1420.
[115] Z. Hu, H. Metiu, Effect of dopants on the energy of oxygen-vacancy formation at the surface of ceria: local or global? J. Phys. Chem. C 115 (2011) 17898–17909.
[116] J. Rogal, K. Reuter, Ab initio atomistic thermodynamics for surfaces: a primer, Exp. Model. Simul. Gas-Surf. Interact. React. Flows Hypers. Flights (2006), 2–1–2–18.
[117] M.W. Chase Jr., NIST-JANAF Thermochemical Tables, 4th Edition, J. Phys. Chem. Ref. Data: Monogr. 9 (1998) 1–1951.
[118] D. Kunwar, S. Zhou, A. DeLaRiva, E.J. Peterson, H. Xiong, X.I. Pereira-Hernández, S.C. Purdy, R. ter Veen, H.H. Brongersma, J.T. Miller, H. Hashiguchi, L. Kovarik, S. Lin, H. Guo, Y. Wang, A.K. Datye, Stabilizing high metal loadings of thermally stable platinum single atoms on an industrial catalyst support, ACS Catal. 9 (2019) 3978–3990.
[119] A. Holmgren, F. Azarnoush, E. Fridell, Influence of pre-treatment on the low-temperature activity of Pt/ceria, Appl. Catal. B: Environ. 22 (1999) 49–61.
[120] X. Ye, H. Wang, Y. Lin, X. Liu, L. Cao, J. Gu, J. Lu, Insight of the stability and activity of platinum single atoms on ceria, Nano Res. 12 (2019) 1401–1409.
[121] J. Jansson, Low-temperature CO oxidation over Co_3O_4/Al_2O_3, J. Catal. 194 (2000) 55–60.
[122] X. Xie, Y. Li, Z.-Q. Liu, M. Haruta, W. Shen, Low-temperature oxidation of CO catalysed by Co_3O_4 nanorods, Nature 458 (2009) 746–749.
[123] Y. Lou, X.-M. Cao, J. Lan, L. Wang, Q. Dai, Y. Guo, J. Ma, Z. Zhao, Y. Guo, P. Hu, G. Lu, Ultralow-temperature CO oxidation on an In_2O_3-Co_3O_4 catalyst: a strategy

to tune CO adsorption strength and oxygen activation simultaneously, Chem. Commun. 50 (2014) 6835–6838.
[124] M. Haruta, T. Kobayashi, H. Sano, N. Yamada, Novel gold catalysts for the oxidation of carbon monoxide at a temperature far below 0 °C, Chem. Lett. 16 (1987) 405–408.
[125] T.S. Kim, J.D. Stiehl, C.T. Reeves, R.J. Meyer, C.B. Mullins, Cryogenic CO oxidation on TiO_2-supported gold nanoclusters precovered with atomic oxygen, J. Am. Chem. Soc. 125 (2003) 2018–2019.
[126] X.-L. Wang, X.-P. Fu, W.-W. Wang, C. Ma, R. Si, C.-J. Jia, Effect of structural evolution of gold species supported on ceria in catalyzing CO oxidation, J. Phys. Chem. C 123 (2019) 9001–9012.
[127] C. Wang, X.-K. Gu, H. Yan, Y. Lin, J. Li, D. Liu, W.-X. Li, J. Lu, Water-mediated Mars–Van Krevelen mechanism for CO oxidation on ceria-supported single-atom Pt_1 catalyst, ACS Catal. 7 (2017) 887–891.
[128] G. Preda, A. Migani, K.M. Neyman, S.T. Bromley, F. Illas, G. Pacchioni, Formation of superoxide anions on ceria nanoparticles by interaction of molecular oxygen with Ce^{3+} sites, J. Phys. Chem. C 115 (2011) 5817–5822.
[129] T. Ohkawa, K. Kuramoto, Theoretical study of CO and O_2 adsorption and CO oxidation on linear-shape gold molecules (LGM_n) (n=2, 4, 8, 16, and 24), AIP Adv. 6 (2016), 095206.
[130] M.W. Roberts, Chemisorption and reactions at metal surfaces, Surf. Sci. 299–300 (1994) 769–784.
[131] D. Hibbitts, E. Iglesia, Prevalence of bimolecular routes in the activation of diatomic molecules with strong chemical bonds (O_2, NO, CO, N_2) on catalytic surfaces, Acc. Chem. Res. 48 (2015) 1254–1262.
[132] W. Dononelli, L.V. Moskaleva, T. Klüner, CO oxidation over unsupported group 11 metal catalysts: new mechanistic insight from first-principles, J. Phys. Chem. C 123 (2019) 7818–7830.
[133] W. Dononelli, G. Tomaschun, T. Klüner, L.V. Moskaleva, Understanding oxygen activation on nanoporous gold, ACS Catal. 9 (2019) 5204–5216.
[134] H.A. Aleksandrov, K.M. Neyman, K.I. Hadjiivanov, G.N. Vayssilov, Can the state of platinum species be unambiguously determined by the stretching frequency of an adsorbed CO probe molecule? Phys. Chem. Chem. Phys. 18 (2016) 22108–22121.
[135] S. Gatla, D. Aubert, V. Flaud, R. Grosjean, T. Lunkenbein, O. Mathon, S. Pascarelli, H. Kaper, Facile synthesis of high-surface area platinum-doped ceria for low temperature CO oxidation, Catal. Today 333 (2019) 105–112.
[136] A.M. Gänzler, M. Casapu, D.E. Doronkin, F. Maurer, P. Lott, P. Glatzel, M. Votsmeier, O. Deutschmann, J.-D. Grunwaldt, Unravelling the different reaction pathways for low temperature CO oxidation on Pt/CeO_2 and Pt/Al_2O_3 by spatially resolved structure–activity correlations, J. Phys. Chem. Lett. (2019) 7698–7705.
[137] F. Pilger, A. Testino, M.A. Lucchini, A. Kambolis, M. Tarik, M.E. Kazzi, Y. Arroyo, M.D. Rossell, C. Ludwig, One-pot polyol synthesis of Pt/CeO_2 and Au/CeO_2 nanopowders as catalysts for CO oxidation, J. Nanosci. Nanotechnol. 15 (2015) 3530–3539.